High-precision earthquake locations in Switzerland using regional secondary arrivals in a 3-D velocity model

Geophysical Journal International

Geophys. J. Int. (2013) **193,** 1589–1607
Advance Access publication 2013 March 07

doi: 10.1093/gji/ggt052

High-precision earthquake locations in Switzerland using regional secondary arrivals in a 3-D velocity model

Michael Wagner,[1] Stephan Husen,[1] Anthony Lomax,[2] Edi Kissling[3] and Domenico Giardini[3]

[1] *Swiss Seismological Service, Swiss Federal Institute of Technology, ETH Zurich,* CH-8092, *Switzerland. E-mail: husen@sed.ethz.ch*
[2] *ALomax Scientific, Mouans-Sartoux, France*
[3] *Institute of Geophysics, Swiss Federal Institute of Technology, ETH Zurich,* CH-8092, *Switzerland*

Accepted 2013 February 5. Received 2013 February 4; in original form 2012 August 8

SUMMARY

We present a new approach to relocate earthquakes in the greater western Alpine region using main crustal phases (*Pg*, *Pn*, *PmP*) that takes advantage of recent developments in *P*-wave velocity models and modelling of the Moho topography in the region, as well as the ability to track reflected and refracted phases in three-dimensional (3-D) heterogeneous media. Our approach includes a new 3-D *P*-wave velocity model for Switzerland and surrounding regions that combines a first-order Moho discontinuity based on local earthquake tomography (LET) and controlled-source seismology (CSS) information and 3-D seismic velocity information based on LET. Traveltimes for the main crustal phases (*Pg*, *Pn*, *PmP*) are computed using a fast marching method. We use a non-linear, probabilistic approach to relocate earthquakes that has been extended to include the use of secondary phases. We validate our approach using synthetic data, which was computed for a real earthquake and different combinations of available phases (*Pg*, *Pn*, *PmP*). We also applied our approach to relocate four selected earthquakes, two shallow and two deep crustal events in the northern Alpine foreland, for which independent information (ground truth information) on their focal depths exist. Our results demonstrate that the precision and accuracy of focal depth estimates can be greatly improved if secondary phases are used. This gain is a combined effect of an improved range of take-off angles and the use of differential traveltimes between first and secondary arriving phases. Our results also show that reliable information on the Moho depth is crucial to obtain accurate focal depths, if *Pn* or *PmP* phases are used in the relocation process. Finally, our approach demonstrates that proper identification of the main crustal phases in combination with an appropriate model parametrization in the forward solver will significantly improve earthquake locations.

Key words: Inverse theory; Seismicity and tectonics; Body waves; Europe.

1 INTRODUCTION

Accurate earthquake locations, and in particular focal depth, are crucial for many seismological studies, such as, for example, hazard assessment and seismic tomography. Furthermore, the distribution of earthquakes in the continental lithosphere, for example, provides important information on its mechanical strength and rheology. The occurrence of earthquakes in the upper crust and uppermost mantle would be in agreement with a more classical rheology of the lithosphere, that is a strong upper crust and mantle lithosphere (e.g. Chen & Molnar 1983). On the other hand, the absence of earthquakes in the upper mantle would favour alternative models of a single, strong, seismically active layer in the crust (e.g. Maggi *et al.* 2000). A key element to distinguish between these two models is the estimation of accurate focal depths with respect to the Moho. Several studies (e.g. Deichmann 1987, 1992; Deichmann & Baer 1990) showed that the European lower crust in the northern Alpine foreland is seismically active, but there is no evidence for a seismically active mantle in this area. In contrast, there exists evidence for a seismically active Adriatic upper mantle in northwestern Italy (e.g. Cattaneo *et al.* 1999). Standard location uncertainties for some of these events, however, are too large to confirm whether they occurred in the crust or in the mantle (Diehl *et al.* 2009a).

The location of an earthquake is a typical ill-posed remote sensing problem where the stations are all situated on the Earth's surface. This is aggravated by the fact that usually only *P* wave and *S* wave first arrival times are used, which leads to an often poorly constrained focal depth. Engdahl *et al.* (1998) showed a significant improvement

in focal depth determination for the teleseismic earthquake location by using teleseismic secondary phases (*pP*, *pwP*, *sP*). Several other studies for individual cases confirmed that secondary arrivals, such as phases reflected from the Moho (*PmP*), increase the accuracy of focal depths in local and regional earthquake location (e.g. Garcia Fernandez & Mayer-Rosa 1986; Deichmann 1987; Kastrup *et al.* 2007). Quin & Thurber (1992) especially highlighted the benefit of *PmP* phases for relocations in a sparse regional network. Some more recent studies (e.g. Stroujkova 2009; Ma 2010) focussed on constraining focal depths by simple waveform modelling for regional depth phases (e.g. *sPg*, *sPmP*, *sPn*) on a more routine basis. All these studies have in common that they either use 1-D or simple 2-D velocity models, which may not be very appropriate for tectonically complex regions as the Alps.

In the northern Alpine region, the *PmP* phase is often well identifiable in the otherwise complex *P* coda due to a highly reflective Moho in the region, and due to a relatively large signal-to-noise (S/N) ratio around the critical distance and an often impulsive onset. This makes it a preferable secondary phase compared to other regional secondary phases usable to constrain focal depth. One main impediment in using *PmP* phases in earthquake hypocentre location is the lack of appropriate velocity models to compute traveltimes of *PmP* phases in 3D. Whereas most 3-D local earthquake tomography (LET) velocity models used for earthquake locations nicely represent lateral variations in seismic velocity, they lack a strong velocity gradient across the Moho discontinuity and this makes it impossible to model Moho reflected phases (e.g. Husen *et al.* 2003). On the other hand velocity models based on controlled-source seismology (CSS) show this strong velocity gradient across the crust–mantle boundary, but they represent simplified and potentially biased 3-D velocity structure due to the necessity of 3-D migration and interpolation between profiles (e.g. Waldhauser *et al.* 2002). In addition, most forward solvers used in earthquake locations are only capable of computing traveltimes of first arriving phases, such as the commonly used finite-difference solver of the Eikonal equations (e.g. Podvin & Lecomte 1991).

Recent developments in *P*-wave velocity models (Diehl *et al.* 2009a) and modelling of the Moho topography (Waldhauser *et al.* 1998; Wagner *et al.* 2012), as well as the ability to track reflected and refracted phases in 3-D heterogeneous media (e.g. de Kool *et al.* 2006; Bai *et al.* 2010) make the greater western Alpine region (Fig. 1) an ideal location to develop a more sophisticated procedure for earthquake hypocentre determination including secondary phases.

In this study, we present a new approach to locate earthquakes in a 3-D crustal velocity model using regional first and secondary phases (*Pg*, *Pn*, *PmP*). We develop our approach for the greater western Alpine region where a highly complex 3-D velocity field with three separate Moho discontinuities exist. Our approach includes a new 3-D *P*-wave velocity model that combines a first-order Moho discontinuity based on combined LET and CSS information (Wagner *et al.* 2012) and 3-D seismic velocity information based on LET (Diehl *et al.* 2009a). Travel times for the main crustal phases (*Pg, Pn, PmP*) are computed using the fast marching method (FMM, http://rses.anu.edu.au/nick/waves.html; Rawlinson & Sambridge 2004a, 2004b, 2005; de Kool *et al.* 2006). We use a non-linear, probabilistic approach to relocate earthquakes (Lomax *et al.* 2000) that has been extended to include secondary phases. We validate our approach using synthetic data, which was computed for a real earthquake, and different combinations of available phases (*Pg, Pn, PmP*). We also applied our approach to relocate four real earthquakes in the northern Alpine foreland—Cortaillod (2006), Basel (2007), Lindau (2004) and Waldburg (2002)—for which independent information (ground truth information, see, e.g. Bondár *et al.* 2001, 2004) on their focal depths exist (Fig. 1). Our results demonstrate that the precision and accuracy of focal depth estimates can be greatly improved if secondary phases are used. Our results also show that reliable information on the Moho depth and topography is crucial to obtain accurate focal depths if *Pn* or *PmP* phases are used in the relocation process.

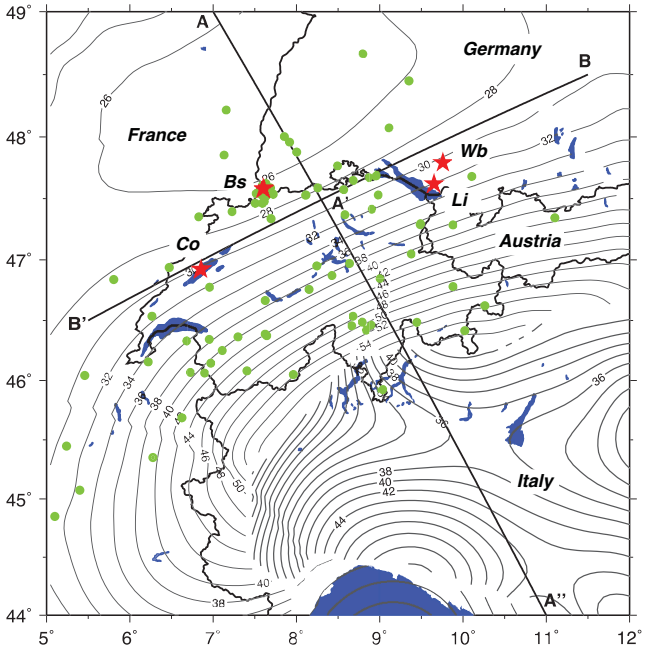

Figure 1. Overview map of the study region. Contour lines denote Moho depth in the western Alpine region (Wagner *et al.* 2012). Contour interval is 2 km. Orientation of profiles shown in this study are shown by black lines (A–A′–A″ and B–B′). Red stars indicate location of real earthquakes discussed in Section 4 (Co, Cortaillod, Bs, Basel, Li, Lindau, Wb, Waldburg). Green dots mark location of seismological stations used in this study.

2 3-D VELOCITY MODEL FOR EARTHQUAKE LOCATION

Velocity models for earthquake location including secondary arrivals need to fulfil several requirements. In particular, they must represent 3-D variations in seismic velocities as well as a first-order Moho discontinuity. Since LET models nicely image 3-D velocity changes, they are often used for earthquake location (e.g. Husen *et al.* 2003), although they do not satisfy all requirements. LET models have a model parametrization that is not suitable for modelling the strong velocity gradient across the Moho discontinuity (e.g. Kissling *et al.* 2001). In contrast, CSS models are specifically designed to image a first-order discontinuity such as the Moho, but due to their profile-based information they usually show only a simplified representation of the 3-D seismic velocity field. Therefore, one needs to merge the information from both methods to obtain a model that fulfils all above-mentioned requirements. For our study region, we are using the LET model of Diehl *et al.* (2009a) and the Moho topography of Wagner *et al.* (2012) which contain the most recent information for this area. In a first step, an initial 1-D reference crustal velocity model is adapted for each *x*/*y* grid node to the appropriate Moho depth. In a second step, LET derived velocity perturbations are added to each velocity–depth string of nodes, thus

completing a 3-D *P*-wave velocity model in accordance both with Moho topography and local velocity variations.

2.1 Initial 1-D reference crustal velocity model

As we subsequently want to add velocity perturbations as derived from LET to the initial 1-D reference model, we need to start from the minimum 1-D model of Diehl *et al.* (2009b, Fig. 2a) that was used to compute the 3-D LET model. In its original form, the minimum 1-D model is a constant-velocity layered model (Kissling *et al.* 1994). Thus, it had to be reparametrized to a velocity gradient model that fits the inversion grid (Fig. 2a). Our 1-D reference model is a representation of this velocity gradient model that additionally was reparametrized to a 2-km vertical grid spacing. As described by Waldhauser *et al.* (2002), this grid spacing is needed to model the strong velocity gradient across the crust–mantle boundary.

Our initial 1-D reference velocity model is a good representation of the normal continental crust with a near-surface crystalline basement structure, upper and lower crust, an averaged Moho depth of 32 km, and a sub-Moho mantle lithosphere velocity of 8 km s^{-1}. With regards to typical lower crustal and uppermost mantle velocities and our 2-km vertical grid spacing, a velocity of 7.25 km s^{-1} best characterizes the depth of the Moho in our 1-D reference model and, therefore, is associated with the closest gridpoint (Fig. 2). This velocity was also used to identify the Moho depth (Wagner *et al.* 2012) in the LET model of Diehl *et al.* (2009a). The grid node above the Moho has a velocity of 6.45 km s^{-1} that describes a lower crustal velocity typical for our study region (Mueller 1977). At the grid node below the Moho, we set the velocity to a value of 8.0 km s^{-1} which is typical for the uppermost mantle. The next deeper gridpoint has a value of 8.05 km s^{-1}, followed by a smooth gradient until a velocity of 8.15 km s^{-1} is reached by adding always 0.01 km s^{-1} to the following gridpoints. This procedure allows for a strong velocity gradient (6.45–8.0 km s^{-1}) over a short distance (4 km) that approximates a first-order discontinuity in our model (Fig. 2a).

To account for the varying Moho depth, the 1-D reference model is adapted in a second step to the local Moho depth (Fig. 2). In this context, two additional cases to the normal one are existing: (i) a shallower Moho (e.g. beneath the Upper Rhine Graben; Fig. 2b) and (ii) a deeper Moho (e.g. beneath the Alps; Fig. 2c). Schmid & Kissling (2000) document a more pronounced increase in lower

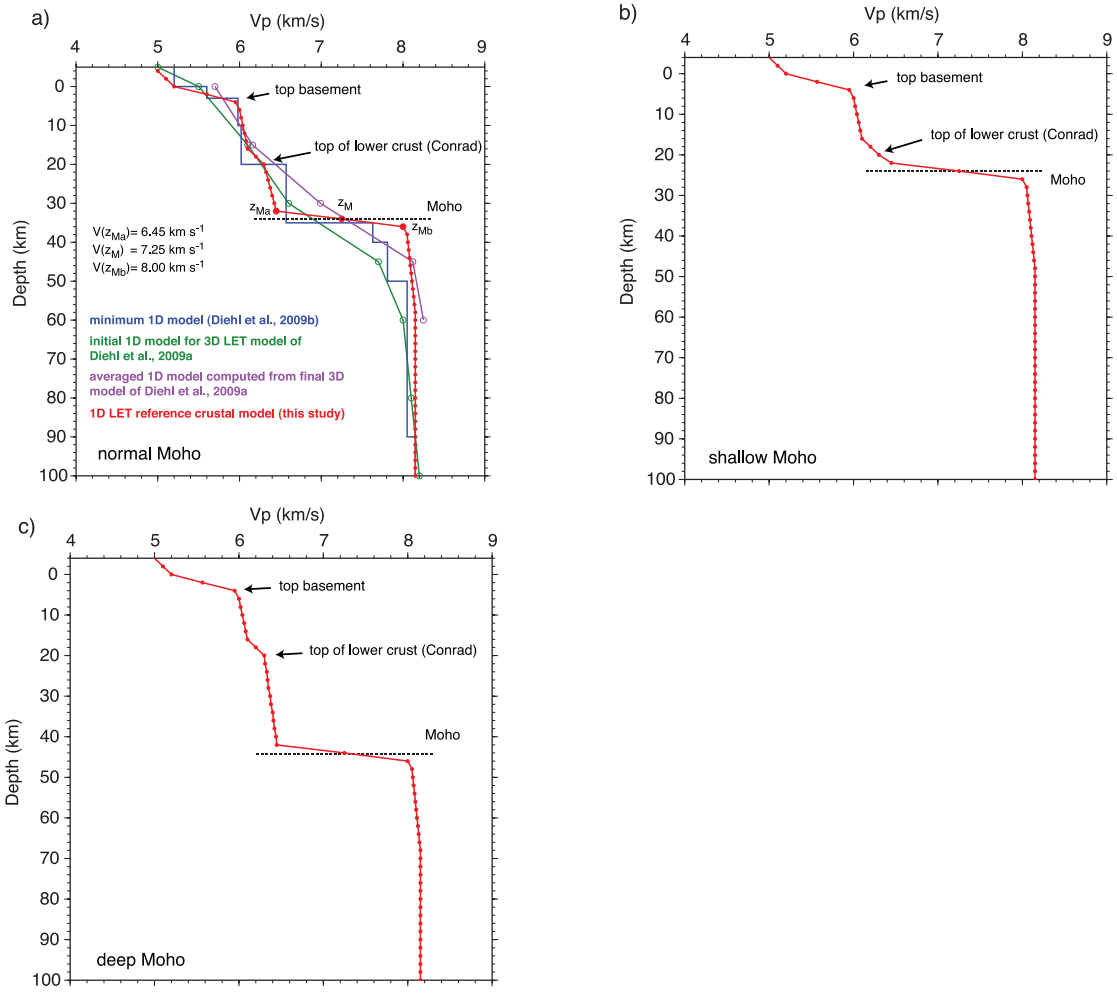

Figure 2. (a) Initial 1-D reference crustal *P*-wave velocity model (red) compared to constant velocity layered minimum 1-D *P*-wave model of Diehl *et al.* (2009b) (blue), initial 1-D *P*-wave model for 3-D LET study of Diehl *et al.* (2009a) (green) and averaged 1-D *P*-wave model computed from final 3-D LET *P*-wave velocity model of Diehl *et al.* (2009a) in well-resolved model parts (violet) for a normal Moho depth. z_{Ma}, z_M and z_{Mb} mark grid nodes just above, at and just below Moho, respectively. These grid nodes have assigned velocities of V(z_{Ma}) = 6.45 km s^{-1}, V(z_M) = 7.25 km s^{-1} and V(z_{Mb}) = 8.00 km s^{-1}, respectively. (b) and (c) Adaption of initial 1-D reference crustal velocity model to a shallow Moho and a deep Moho, respectively. See text for more details on how initial 1-D crustal *P*-wave velocity model has been computed.

crustal thickness than in upper crustal thickness beneath the Alps. This effect is utilized in the adaptation of the 1-D reference model by keeping the depth to top basement and the thickness of upper crust fixed and adjusting the lower crustal thickness to fit the Moho depth (Fig. 2).

2.2 Final 3-D crustal velocity model

The final 3-D crustal *P*-wave velocity model for earthquake location is established by updating the initial 1-D reference crustal velocity model (see Section 2.1) with lateral velocity variations of the 3-D LET model of Diehl *et al.* (2009a). A diagonal element of the resolution matrix (RDE) of 0.05 denotes the lower limit of poorly to fairly well-resolved cells in the LET model of Diehl *et al.* (2009a) and was chosen as requirement for updating the 3-D velocity field. To avoid unrealistic local velocity anomalies, particularly from the less well-resolved model cells, local relative velocity changes are limited to a maximum of ±5 per cent. For an average upper crustal velocity of 6 km s^{-1}, this limit covers the range from 5.7 to 6.3 km s^{-1} and for an average lower crustal velocity of 6.4 km s^{-1} a range from 6.1 to 6.7 km s^{-1}. Considering the cell size of 25 km × 25 km × 15 km in the LET model (Diehl *et al.* 2009a), this covers all crustal structure except near-surface sedimentary basins or the geophysical Ivrea body (Kissling 1993). The latter is included in our Moho topography model (Wagner *et al.* 2012). While the velocity effects of the sedimentary basins are included in the average velocity of the surface LET cells, the detailed structure, that is topography of the top basement, in these cases are not taken into account in our 3-D crustal model. The comparison between the 3-D LET *P*-wave velocity model of Diehl *et al.* (2009a) and our final 3-D crustal *P*-wave velocity model for earthquake location reveals the strong similarities in the 3-D crustal velocity field with a distinctively improved very strong velocity gradient across the Moho (Fig. 3). Note that local anomalies of relatively low near-surface velocities beneath the Upper Rhine Graben, the Molasse Basin and the Po Plain compare just as well as intracrustal velocity variations beneath the Alps (Fig. 3). In the parts where the LET model is poorly resolved, our 3-D crustal *P*-wave velocity model stays close to our initial 1-D reference model with adjusted Moho depth (Fig. 3).

3 EARTHQUAKE HYPOCENTRE DETERMINATION

In the following section, we give detailed information about non-linear earthquake hypocentre determination including secondary phases. We start with the description of the non-linear approach and the advantages of using the equal differential time (EDT) likelihood function (Font *et al.* 2004; Lomax 2005). Thereafter, we introduce how the FMM is used to compute arrival times of main crustal phases (*Pg*, *Pn*, *PmP*) for earthquake location. Finally, we conclude by investigating the influence of secondary arrivals on earthquake location accuracy and precision by means of tests with synthetic data.

3.1 Non-linear approach

In our study, we are using the NonLinLoc software package (Lomax *et al.* 2000, http://alomax.free.fr/nlloc/) to compute the posterior probability density function (PDF) of the location problem. The PDF represents a complete, probabilistic solution to the location problem. The solution is fully non-linear and, therefore, the resulting PDF may be irregular and multimodal. Another advantage of NonLinLoc is its ability to use the EDT likelihood function that is much more robust in the presence of outliers than the usual, rms, L2 norm (Font *et al.* 2004; Lomax 2005). In NonLinLoc, the PDF using the EDT likelihood function has the following form (Lomax 2005):

$$PDF(\mathbf{x}) \propto k\left[\sum_{obs_a,obs_b} \frac{1}{\sqrt{\sigma_a^2+\sigma_b^2}} \exp\left(-\frac{\{[T_{\mathrm{obs}_a}(\mathbf{x})-T_{\mathrm{obs}_b}(\mathbf{x})]-[TT_{\mathrm{calc}_a}(\mathbf{x})-TT_{\mathrm{b}}(\mathbf{x})]\}^2}{\sigma_a^2+\sigma_b^2}\right)\right]^N. \quad (1)$$

Given two observations obs_a and obs_b, T_{obs_a} and T_{obs_b} are their observed arrival times and TT_{calc_a} and TT_{calc_b} their calculated arrival times, respectively. σ_a and σ_b are the assigned errors of the two observations. k is a normalization factor and N the total number of observations. In eq. (1), the sum is taken over differential times between observed and calculated traveltimes of all pairs of observations. Pairs of observations that result in a zero differential time attribute to points **x** that best satisfy the two observations. Sets of points **x** where the differential time is non-zero build a finite width, curved 3-D surface in space. Eq. (1) reaches its highest values where the most pairs of observations are satisfied. Therefore, the EDT likelihood function is less sensitive to outlier data (Lomax 2005). This becomes especially important if secondary phases are used in the location process. The identification of secondary phases in a seismogram can be difficult due to complex velocity structure and focusing and defocusing effects, which lead to misidentification (e.g. secondary *Pg* instead of *PmP*). The usage of secondary phases within the NonLinLoc software package is easily introduced by considering their corresponding traveltime fields.

In the presence of outlier data, the PDF using the EDT likelihood function can have a highly complex and irregular topology which requires efficient and stable global sampling algorithms to correctly compute the PDF. In our study, we are using the oct-tree importance sampling method, which has been proven to work well with the EDT likelihood function (Lomax 2005).

3.2 Calculation of traveltimes

In the NonLinLoc software package (see above), traveltimes between each station and all nodes of a spatial grid are calculated using the Eikonal finite-difference scheme of Podvin & Lecomte (1991) (hereafter PL91). This algorithm uses a finite-difference approximation of Huygen's principle to find the first arriving traveltimes at all grid nodes of a 3-D Cartesian grid.

Tracking of reflected waves is quite complicated with the algorithm of PL91 as it normally computes only first arriving traveltimes. The PL91 procedure requires regular, cubic grids that will not only lead to very large arrays when a fine grid spacing is needed, but also result in a step-like representation of the Moho discontinuity. Another drawback of PL91 is its restriction to first-order solutions of the Eikonal equation. Therefore, we decided to apply a different approach for the computation of traveltimes. Among various conventional ray tracing and grid-based methods (e.g. Bai *et al.* 2010) for traveltime calculations, we choose the well developed and freely available multistage FMM procedure for complex layered media (Rawlinson & Sambridge 2004a, 2005; de Kool *et al.* 2006). It is still a grid-based numerical scheme for computing seismic

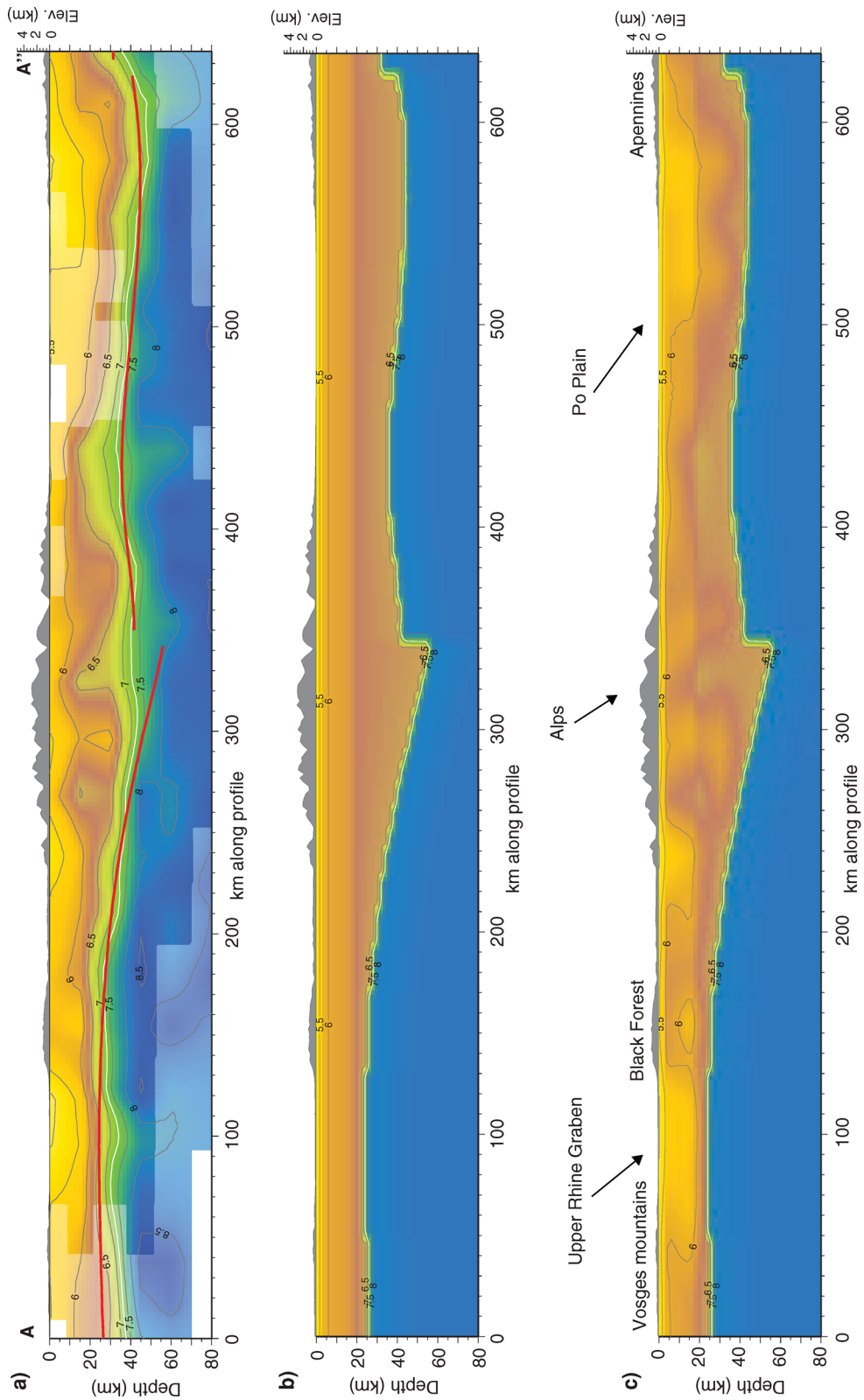

Figure 3. Vertical cross-section through (a) 3-D LET *P*-wave model of Diehl *et al.* (2009a), (b) initial 1-D reference crustal *P*-wave velocity model and (c) final 3-D *P*-wave velocity model for earthquake relocation. Shaded colours in (a) outline areas of poor resolution. Areas with very poor ray coverage in (a) are shown in white. Thick red line in (a) shows Moho depth along profile (Wagner *et al.* 2012). For orientation of profiles, see Fig. 1. Note good match in the pattern of high and low *P*-wave velocities in the 3-D LET *P*-wave model and final 3-D *P*-wave velocity model for earthquake relocation between profile kilometres $x = 240$ km and $x = 440$ km. In poorly resolved regions of the 3-D LET *P*-wave model, the final 3-D *P*-wave model for earthquake location is close to the initial 1-D reference crustal *P*-wave model (e.g. between profile kilometres $x = 0$ km and $x = 40$ km).

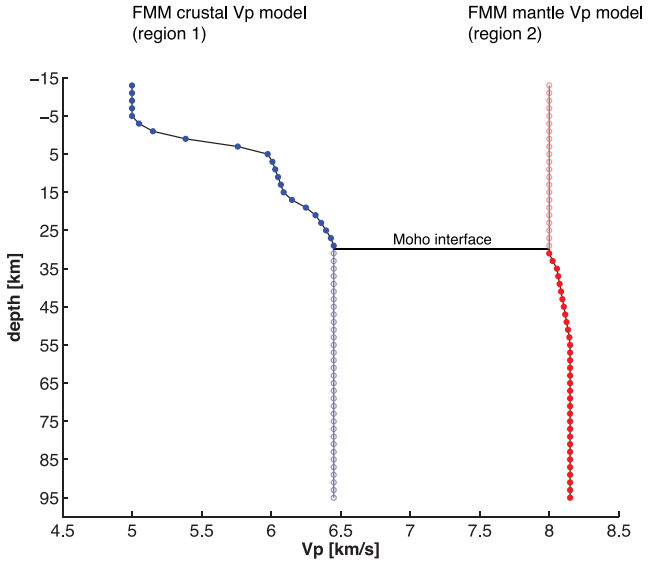

Figure 4. Model parametrization for fast marching method. The Moho interface at $z = 30$ km separates the velocity model for earthquake location into a crustal *P*-wave velocity model (region 1) and a mantle *P*-wave velocity model (region 2). *P*-wave velocities in each model are continued below and above Moho as indicated, respectively. See text for more details on how model parametrization is adapted for 3-D Moho.

traveltimes based on the finite-difference solution of the Eikonal equation. In the multistage FMM procedure interfaces separate different regions of laterally and vertically variable velocities (Fig. 4). Thus, each region is considered as a separated computational domain. A wave front is propagated through a region until all points of the interface are reached. A reflected wave front can then be tracked by reinitializing FMM from the interface back into the incident region. Similarly, a transmitted wave front can be tracked by reinitializing FMM into the adjacent region (Rawlinson & Sambridge 2004a; de Kool *et al.* 2006). So-called path sequences are defined based on the travel path of a certain phase (e.g. *Pg*, *Pn*, *PmP*). These path sequences are then used to efficiently compute the traveltimes of the individual phases.

The FMM procedure uses three different grids for computation, called 'velocity', 'interface' and 'propagation grid' (Rawlinson & Sambridge 2004a; de Kool *et al.* 2006). The velocity grid defines seismic velocities on a regularly spaced 3-D grid in spherical coordinates. The interface grid specifies the location of interfaces, for example, Moho, at depth. It can be irregularly spaced in depth to account for complex interface topographies (Fig. 5). The regularly spaced propagation grid is used for computation of traveltimes. The Moho interface divides the propagation grid into a crustal and mantle region. Traveltimes are computed within each region on all nodes of the propagation and interface grid but only traveltimes on nodes of the regularly spaced propagation grid are saved to disk. This means that for crustal phases, such as *Pg*, *Pn* or *PmP*, traveltimes are only available at grid nodes above the Moho, excluding grid nodes along the interface (Fig. 5).

We use the Moho interface developed by Wagner *et al.* (2012) to separate our 3-D velocity model for earthquake location (as described in Section 2.2) into a crustal and a mantle region (Fig. 4). As mentioned earlier, those two regions are treated separately in the FMM procedure and, thus, make it possible to model a true first-order discontinuity between crust and mantle (Fig. 4). In this context, a correct separation of the crustal velocities above the Moho interface and the mantle velocities below the Moho interface

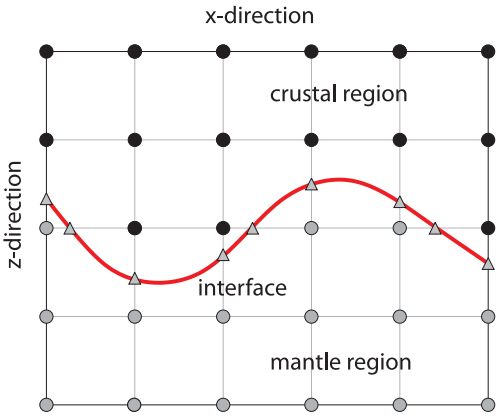

Figure 5. Sketch (2-D) of different grids used in the FMM procedure. Circles denote location of grid nodes of the regularly spaced velocity and propagation grid. In this example, grid nodes of the velocity and propagation grid are identical. Red line and grey triangles mark location of interface, for example, Moho, that separates the velocity and propagation grid into a crustal and mantle region. For crustal phases, such as *Pg, Pn, PmP*, only traveltimes computed on grid nodes above the interface (black circles) are saved to disk (modified after Rawlinson & Sambridge 2005). See text for more details on the meaning of the different grids.

are essential to avoid a velocity gradient smoothing the first-order discontinuity and, thus, annihilating the *PmP* reflection. As the 3-D velocity model for earthquake location is calculated on a (6 km × 6 km × 2 km) 3-D Cartesian grid, it is essential to transform it into an FMM definition that allows for exactly the same velocity interpolation. To reduce artefacts introduced by different interpolation schemes (i.e. linear interpolation for 3-D velocity model and *B*-spline interpolation for FMM grids) (Haslinger & Kissling 2001), spacing of the grid nodes of the velocity and propagation grid is set to 2 km in horizontal and vertical direction. This results in a total number of more than $3.5 \cdot 10^6$ grid nodes for the whole model area. The same grid node spacing (2 km × 2 km) is used for the 2-D interface grid.

Determination of traveltimes of crustal phases along specific profiles is a common procedure in CSS. We did a similar test to prove the correct identification and calculation of *Pg*, *Pn* and *PmP* phases with the FMM and the chosen model parametrization. Along a profile running parallel to the strike of the Alps, that is with a simple (almost constant) Moho topography (Fig. 6a), we show wavefields (Fig. 6b) and traveltime curves (Fig. 6c) of *Pg*, *Pn* and *PmP* phases through our initial 1-D reference crustal model (Fig. 6 d). As mentioned in Section 2.1 no lateral variations in seismic velocities are represented in the initial 1-D reference crustal model. The additional simple Moho topography along the chosen profile allows a relative easy recognition of traveltimes branches known from active seismics. Based on the traveltime curves (Fig. 6c), we clearly identify the *Pg*, *Pn* and *PmP* phase as well as a crossover distance at about 140 km along profile that is realistic with the given velocity model and a Moho depth of about 30 km along profile. Before the traveltimes of the *Pg* and *PmP* phase merge, we see an unusual deviation from the horizontal of the *Pg* and *PmP* phase at about 180 km (Fig. 6c). Using a traditional ray tracing software (MacRay, Luetgert 1992), we could confirm this behaviour that is due to a refraction of the direct wave in the lower crust. The unrealistic arrival times of the *Pn* phase for distances within the critical distance is due to the fact that FMM solves the mathematical problem to compute *Pn* traveltimes without considering the physical condition that no *Pn* is generated closer to the source than in the critical distance.

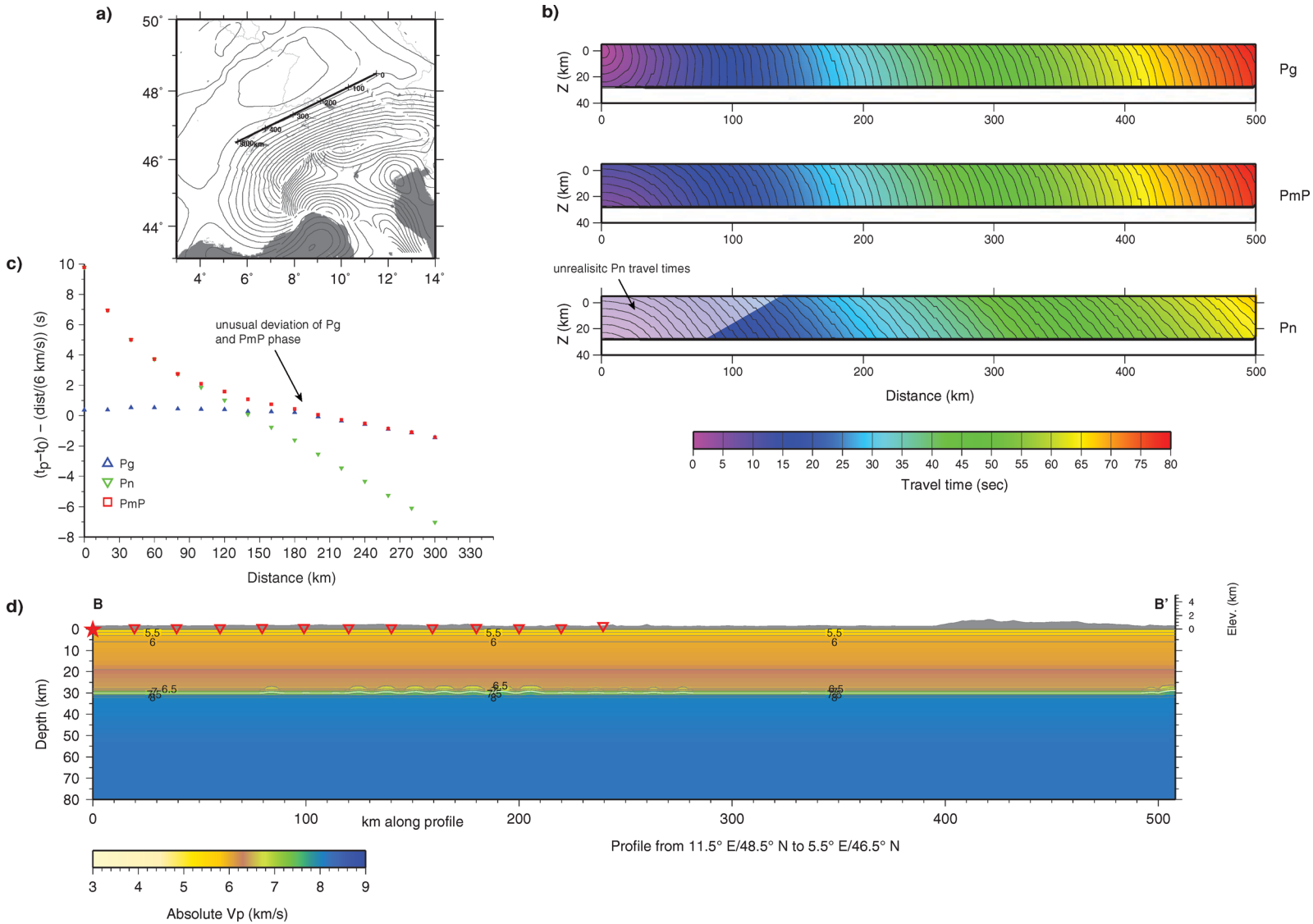

Figure 6. Computation of traveltimes of main crustal phases (*Pg, Pn, PmP*) in initial 1-D reference crustal *P*-wave velocity model using fast marching method. (a) Orientation of profile and Moho depth in the greater Alpine region. (b) Traveltime fields of *Pg, Pn* and *PmP* phases. Colours denote traveltime in seconds as indicated. Contours show wave fronts at 1 s intervals. Unrealistic *Pn* traveltimes are shaded. Note that traveltime fields are only defined above Moho interface. (c) Reduced traveltime curves of *Pg, Pn* and *PmP* phase along profile. Reduction velocity is 6 km s^{-1}. (d) Vertical cross-section through initial 1-D reference crustal *P*-wave velocity model. Red star at 0 km depth marks position of source. Red triangles exemplarily show position of receivers. For discussion of results, see text.

In Fig. 6(b), the corresponding wavefields are shown. Similar to the traveltime curves we see that the *Pg* and *PmP* phase have different wavefields close to the source. At distances beyond about 200 km, their wavefields become almost identical. The wavefield of the *Pn* phase shows its typical behaviour of being secondary arriving till the crossover distance when overtaking the *Pg* phase. Moreover, it is nicely seen that the *Pn* is propagating with a different angle of incidence than *Pg* and *PmP*. With this test we could not only prove the correct computation of traveltimes, but also demonstrate that tracing of the wave fronts done by FMM can be used in a similar way as it is, for example, done by Kastrup *et al.* (2007) who used 2-D ray tracing along specific profiles to better constrain focal depth of individual earthquakes.

In a second test, we show the capability of using FMM for calculating traveltimes of crustal phases for a much more complicated, but realistic setup. Now we examine the traveltimes and wavefields of crustal phases through our 3-D velocity model. Starting from a 25-km deep source in northern Switzerland the profile runs perpendicular to the strike of the Alps in southeastern direction towards the Apennines (Fig. 7). Along the profile the Moho is deepening from about 30 to about 55 km beneath the Alps, followed by an offset of about 15 km and a gently shallowing and deepening (Figs 7a and d). The traveltime curves (Fig. 7c) reflect the complex Moho topography. The direct wave is now an upgoing wave from a source in the lower crust and, thus, called *Pb* (Storchak *et al.* 2003). Since the traveltimes of the *Pb* and *PmP* phase are close together and the amplitude of both phases at nearby stations has a similar magnitude, in reality it is often difficult to distinguish between both phases. With the additional *Pn* phase it gets even more complicated in the triplication zone, while at greater distances the *Pn* clearly is the first arriving phase, though of a relatively low S/N ratio. In addition, we note a bump in the traveltime curves of the *Pb*, *PmP* and especially *Pn* phase between 140 and 270 km (Fig. 7c) due to the distinct Moho topography across the plate boundary at 140 km in the model (Fig. 7d). As mentioned in the previous paragraph, *Pn* phases within the critical distance are also existent in the mathematical solution of FMM, though unrealistic. Fig. 7(b) illustrates the wavefields of the *Pb*, *PmP* and *Pn* phase. Whereas the *Pb* and *PmP* wavefields are similar the wavefield of the *Pn* phase is clearly distinguishable from the others and shows, along with a different propagation angle, shorter traveltimes from around 140 km and, hence, is then the first arriving phase.

Further validations of our newly developed approach are based on a comparison of earthquake locations using the PL91 and FMM scheme for the forward calculation (Fig. 8). The test is based on a real earthquake and station distribution (2006 Cortaillod earthquake). The same velocity model and observations (including traveltime errors) are used for the PL91 and FMM approach. Since both methods are different in terms of model parametrization and computation of arrival times (see above), we try to minimize these effects by using only direct *Pg* phases observed at nearby stations that are not influenced by the Moho. In Fig. 8, we can see that there is a good agreement between the PL91 and FMM hypocentre location. Both methods reveal similar locations within their uncertainties. The scatter density clouds (a representation of the location PDF) of both locations are overlapping. Moreover, the rms of the residuals at the maximum likelihood location has a similar value, that is a very small difference of less than 0.018 s, for both approaches and, furthermore, is smaller than the assumed final rms traveltime residuals in the model of Diehl *et al.* (2009a). In conclusion, we can say that these findings are an additional confirmation that reliable results are derived with the FMM approach.

3.3 Effect of secondary phases on hypocentre determination

To investigate the influence of secondary phases on the earthquake location, we performed several relocation tests (Table 1). These tests are based on the real location and distribution of stations of the Cortaillod earthquake. Using our newly developed 3-D crustal velocity model, we calculated traveltimes for *Pg*, *Pn* and *PmP* phases. No randomly distributed traveltime errors were added, but a formal uncertainty of ± 0.1 s was used to compute the PDF. We divided the tests in two different categories: (i) generic and (ii) true distribution. The former refers to tests with all possible combinations of different phases (*Pg*, *Pn*, *PmP*), whereas the latter uses the observed distribution of phases for the Cortaillod earthquake. The half-axes of the 68 per cent confidence ellipsoid are used to assess location uncertainties in x, y, z directions, which is possible due to mostly vertical orientation of the ellipsoid.

The generic setup contains all possible combinations of *Pg*, *Pn* and *PmP* phases to investigate the influence of each phase type and their combination on the location problem. To allow a fair comparison, we compute traveltimes for each phase and all stations, where they potentially exist. This, for example, yields the same number of *Pg* and *PmP* phases for distances within and beyond the critical distance (Table 1). Since this setup does not correspond to a realistic distribution of *Pg*, *Pn* and *PmP* phases we call it generic. Taking the *Pg* location as a reference, we see a decrease in the vertical location uncertainty ('len3' in Table 1) by a factor of around 3 when adding *Pn* or *PmP* phases to the *Pg* phases which is also coupled to a decrease in the horizontal location uncertainty ('len1' and 'len2' in Table 1). Using all three types of phases together does only slightly further reduce the location uncertainty. To further investigate the influence of different phases on the location result, we compared relocation results obtained using only *Pg* or *PmP* phases within and beyond the critical distance, respectively. Table 1 shows that similar results are obtained whether only *Pg* or *PmP* phases are used. Results using phases within and beyond critical distance cannot directly be compared to each other due to a too different number of observations.

Our generic tests show that using each phase separately yields similar relocation results, for example, the use of *Pg* or *PmP* phases at distances within the critical distance yields similar relocation results. This indicates that all phases can be given the same weight in the relocation process. They should only be weighted according to their assigned observational uncertainty. Our results further demonstrate that the combination of different phases (e.g. *Pg* and *PmP* or *Pg* and *Pn*) significantly reduce location uncertainty. Thereby, it is important to note that not any combination in preferred. They all result in a location accuracy and precision of a similar magnitude (Table 1). The documented improvement in the determination of the earthquake hypocentre, especially focal depth, results from two reasons: First, improvements in the distribution of take-off angles, for example, by adding *Pn* phases or *PmP*s within the critical distance and, secondly, availability of differential traveltimes of different phases at the same station, for example, by using *Pg* and *PmP* phases at the same station. The former reason is comparable to the effect of adding *S* phases which adds a different range of take-off angles to the location problem due to slower *S*-wave velocities (Gomberg *et al.* 1990). Considering picking of secondary phase onsets with weak signal amplitudes or in general low S/N ratios, *PmP* phases may be a good choice to improve determination of focal depth, because they often show high signal amplitudes and,

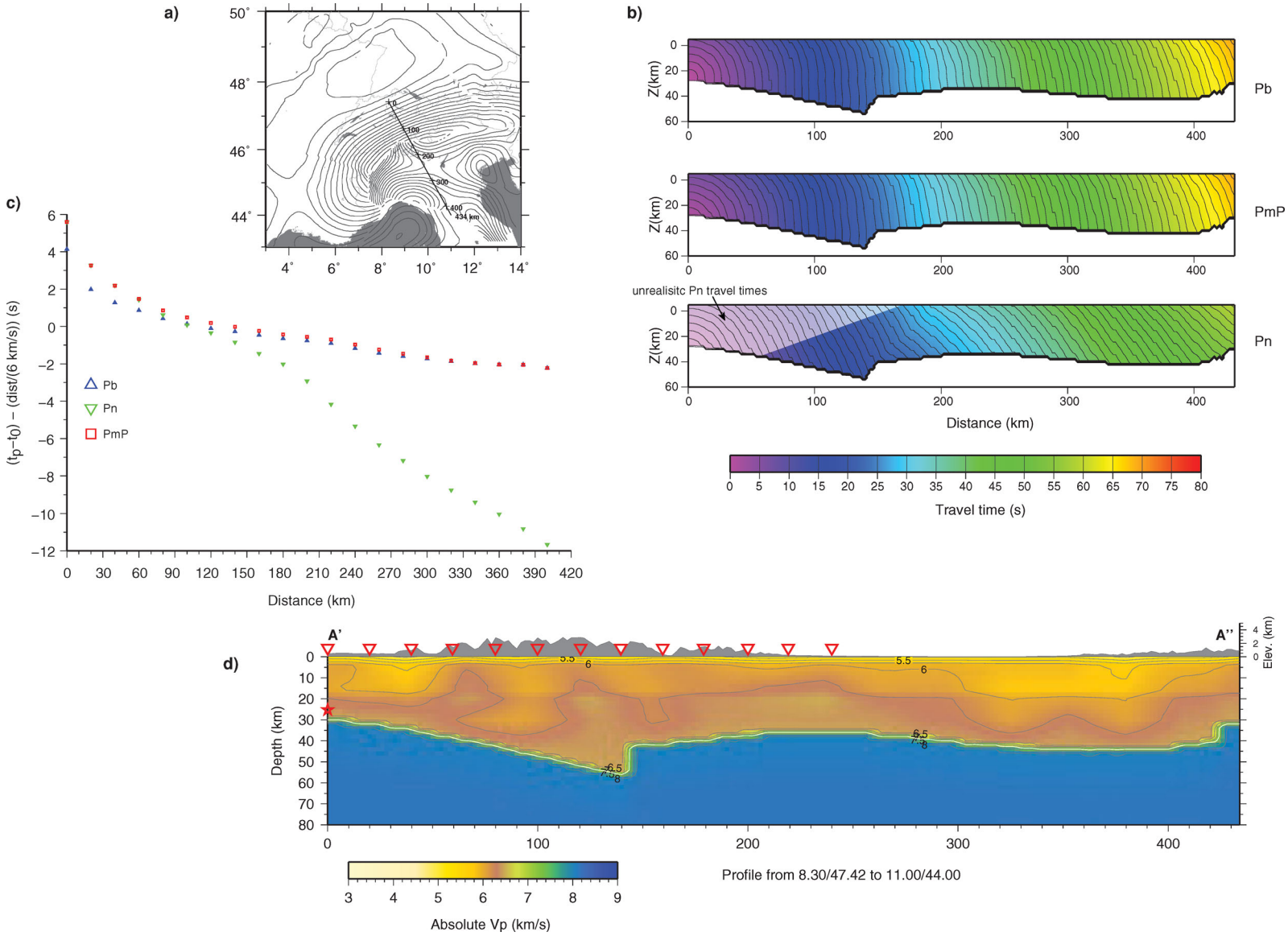

Figure 7. Same as Fig. 6, but for final 3-D *P*-wave velocity model for earthquake relocation and a deep crustal source.

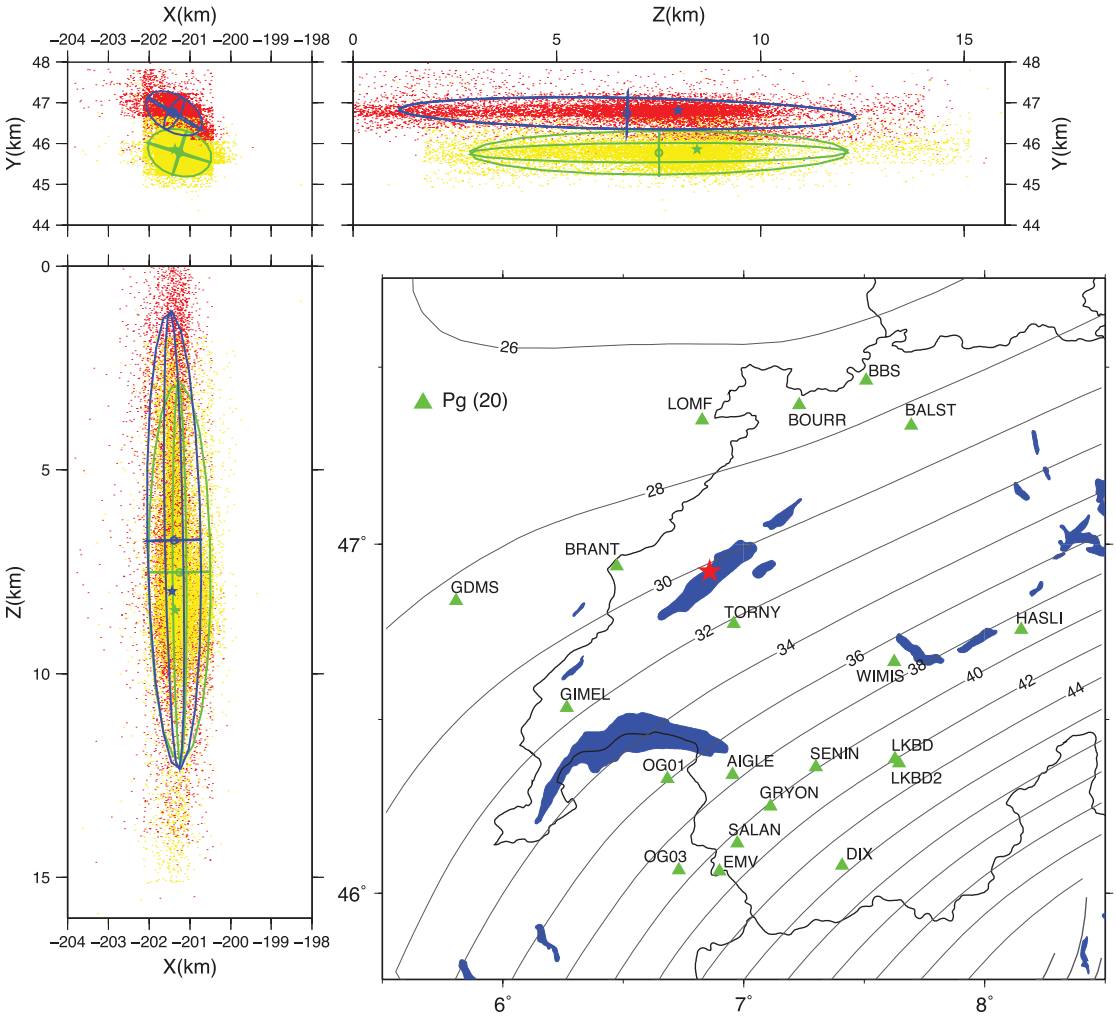

Figure 8. Posterior probability density function shown as density scatterplots for the Cortaillod earthquake computed using finite-difference solution of the Eikonal equations (PL91; Podvin & Lecomte 1991) (red) and fast marching method (FMM; de Kool *et al.* 2006) (yellow). Horizontal plane view and vertical cross-section in *x*-*z* direction and *y*-*z* direction are shown. Stars mark maximum likelihood locations. Projection of the 68 per cent confidence ellipsoids of each solution are shown by coloured lines: blue, PL91 solution; green, FMM solution. For each solution, root-mean-square of the residuals at the maximum likelihood location (rms), number of phases (Nphs), largest azimuthal gap in station distribution (Gap), distance of closest station to maximum likelihood epicentre location (Dist), length of the half-axes of the 68 per cent confidence ellipsoid (len1, len2, len3) and coordinates of maximum likelihood location (*x*, *y*, *z*) are indicated. Map in the lower right corner shows earthquake epicentre (red star), the distribution of stations (green triangles) and the Moho depth as 2 km contoured lines. Note that both solutions agree very well within their uncertainties.

thus, show a clear phase onset. Examples of using *PmP* phases to improve focal depth estimates are given in Section 4.

Since the setup of our generic test leads to an unrealistic number and distribution of phases, we performed a second test with synthetic traveltimes using the observed number and distribution of phases of the 2006 Cortaillod earthquake (Baer *et al.* 2007). The results of this setup are labelled as 'true distribution' in Table 1. Due to a limited range of take-off angles, the largest uncertainties, especially in focal depth, are observed when only *Pg* phases are used. As mentioned earlier, increasing the range of take-off angles and/or adding differential traveltimes of different phases at the same station improves accuracy and precision of the earthquake location. For the setup of the Cortaillod earthquake, this yields to an improvement of a factor of 4–8 in accuracy (difference between true and relocated hypocentre location) and of about 4 in precision ('len3' in Table 1).

In a second series of tests, we explore the importance of using a correct velocity model and Moho depth for earthquake location (Table 2). Number and distribution of phases is the same as described above for the setups 'generic' and 'true distribution'. Instead of using the same 3-D velocity model for relocation we are now using a velocity model with a 3-km deeper Moho without updating the previously determined synthetic traveltimes. The shift of the Moho depth to a 3-km deeper value is a quite realistic assumption as it is in the range of its error estimation (Waldhauser *et al.* 2002). However, we simulate a systematic shift that is not the same as local Moho depth uncertainties.

Although we are using a wrong velocity model, we receive almost the same 68 per cent confidence ellipsoids compared to the correct velocity model (Tables 1 and 2). In the case of using *Pg* within the critical distance they must be and are identical since crustal velocities were not changed. Overall, this demonstrates that the precision of the earthquake location, as given by the 68 per cent confidence ellipsoid, is not affected by using a wrong velocity model and Moho depth for relocation. At the same time, we observe a difference in focal depth between the maximum likelihood hypocentre of these locations and the true location of the earthquake of up to −8 km

Table 1. Synthetic relocation tests to investigate the influence of secondary phases. The same velocity model (final 3-D *P*-wave velocity model for earthquake location) was used to compute synthetic traveltimes and for relocation. No errors were added to synthetic traveltimes. True location of earthquake is at $x = -202.020$ km, $y = 47.030$ km, $z = 2.000$ km. Number of phases is shown for each phase separately. Difference in x, y and z direction (diff x, diff y, diff z) is calculated between true location and relocated maximum likelihood hypocentre. Lengths of the half-axes of the 68 per cent confidence ellipsoids are given by len1, len2, len3. See text for discussion of results.

Setup	Type of phases	No. of phases	diff x (km)	diff y (km)	diff z (km)	len1 (km)	len2 (km)	len3 (km)
generic								
	Pg	51	0.009	−0.014	0.019	0.232	0.338	1.749
	Pg + *Pn*	51 + 38	0.009	−0.014	0.010	0.192	0.280	0.617
	Pg + *PmP*	51 + 51	0.001	0.002	0.000	0.173	0.260	0.638
	Pg + *Pn* + *PmP*	51 + 38 + 51	0.009	−0.014	0.010	0.155	0.234	0.525
	Pg beyond crit. dist.	38	0.027	−0.032	0.050	0.280	0.446	2.368
	PmP beyond crit. dist.	38	0.027	−0.032	−0.073	0.319	0.545	3.547
	Pg within crit. dist.	13	0.063	0.004	−0.012	0.618	0.695	5.506
	PmP within crit. dist.	13	0.063	0.004	0.093	0.943	1.099	5.797
true distribution								
	Pg	22	0.027	−0.032	0.085	0.374	0.480	4.359
	Pg + *PmP*	22 + 11	0.009	−0.014	0.010	0.293	0.406	1.140
	Pg + *Pn*	22 + 20	0.009	−0.014	0.019	0.268	0.387	0.893
	Pg + *Pn* + *PmP*	22 + 20 + 11	0.009	−0.014	0.010	0.244	0.361	0.802

Table 2. Same as Table 1, but a velocity model with a Moho depth systematically shifted to greater depth (3 km) was used for relocation. See text for discussion of results.

Setup	Type of phases	No. of phases	diff x (km)	diff y (km)	diff z (km)	len1 (km)	len2 (km)	len3 (km)
generic								
	Pg	51	0.206	0.004	−3.788	0.258	0.364	2.735
	Pg + *Pn*	51 + 38	0.206	−0.141	−5.852	0.215	0.323	0.436
	Pg + *PmP*	51 + 51	0.259	−0.123	−5.532	0.200	0.310	0.457
	Pg + *Pn* + *PmP*	51 + 38 + 51	0.295	−0.232	−5.769	0.178	0.278	0.382
	Pg beyond crit. dist.	38	0.170	−0.032	−4.601	0.312	0.499	2.213
	PmP beyond crit. dist.	38	0.241	−0.250	−4.636	0.354	0.596	3.531
	Pg within crit. dist.	13	0.063	0.004	−0.012	0.618	0.695	5.506
	PmP within crit. dist.	13	0.491	−0.722	−8.160	1.027	1.144	5.882
true distribution								
	Pg	22	0.027	−0.032	0.085	0.374	0.480	4.359
	Pg + *PmP*	22 + 11	0.116	−0.087	−5.393	0.320	0.451	0.819
	Pg + *Pn*	22 + 20	0.081	−0.050	−5.917	0.285	0.432	0.596
	Pg + *Pn* + *PmP*	22 + 20 + 11	0.152	−0.123	−5.769	0.260	0.402	0.556

('diff z' in Table 2), which proves that the accuracy of the location is now very poor. The two examples where *Pg* phases propagate only in the upper crust ('*Pg* within crit. dist.', generic and *Pg*, true distribution in Table 2) are the only locations showing the correct hypocentre location, although their precision is one of the worst. Our tests demonstrate that the use of a wrong velocity model or Moho depth will yield hypocentre locations that are systematically biased, even if differential traveltimes between different phases (e.g. *Pg* and *PmP* or *Pn* and *PmP*) are used. Since location precision remains unaffected the systematic bias remains undetected unless the true hypocentre location is known.

4 RELOCATION OF SELECTED EARTHQUAKES USING SECONDARY PHASES

In this section, we apply our newly developed method to real earthquakes. To document the possibilities of earthquake location including secondary arrivals, we compare our results to those of other studies. This could be seen in a similar manner as, for example, the usage of ground truth information for calibration of earthquake location in global seismology (e.g. Bondár *et al.* 2001, 2004). A great advantage of using the NonLinLoc software package in our approach is that we can give detailed information about location uncertainties that are often neglected or simplified when using other location algorithms. Though, we do not further discuss the question of consistent phase identification, we want to mention that in our case all phases were identified and picked by an experienced seismologist (see, e.g. Deichmann *et al.* 2008). In addition, we checked traveltime onsets with the help of velocity reduced traveltime plots that are very useful to verify phase identification (see, e.g. Fig. 9).

As examples we chose four different earthquakes in the northern Alpine foreland. Two of them are very shallow events (at approximately 2 and 4–5 km depth) and the other two events occurred at great depth (around 30 km) close to the Moho discontinuity. In the following order, we discuss the location results of the Cortaillod (2006), Basel (2007), Lindau (2004), and Waldburg (2002) events (Fig. 1). Besides the existing information from other studies, we chose these events due to the following reason: They all occurred at the periphery of the seismic network, which in general makes accurate location more difficult and, therefore, shows what one might gain in such situations following our approach. Especially, the Waldburg event has a very poor network geometry and only

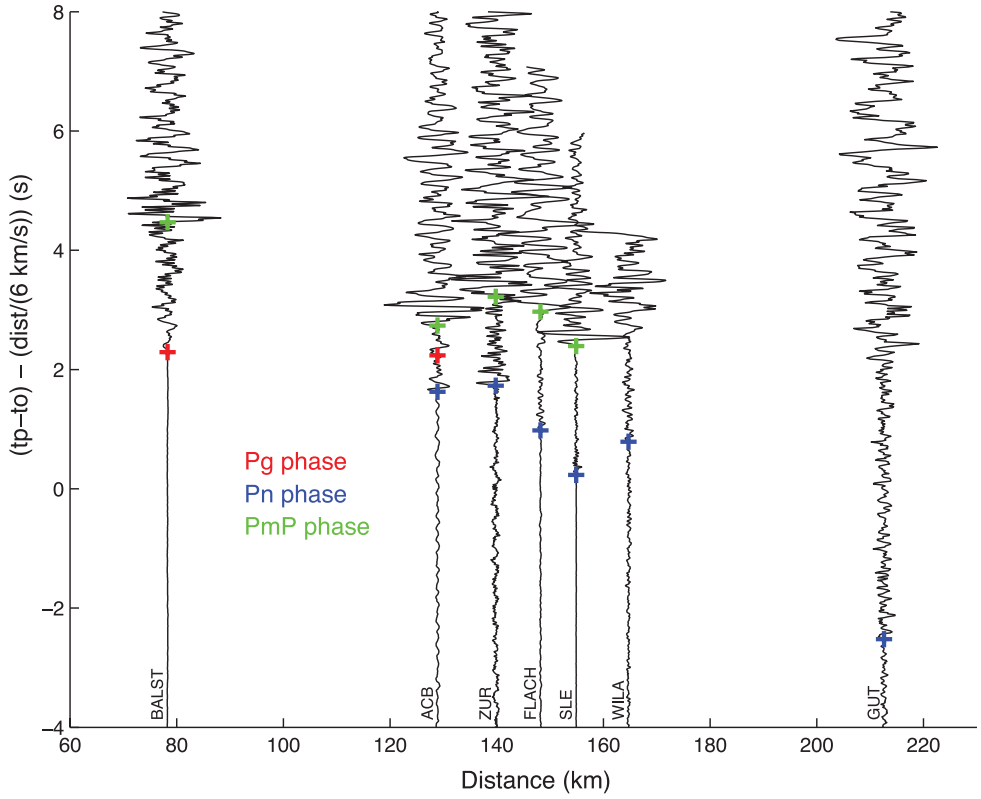

Figure 9. Reduced traveltime section showing seismograms and arrival times of *Pg*, *Pn* and *PmP* phases for the Cortaillod event observed at stations to the NE (azimuth 50°–70°) of the epicentre. Reduction velocity is 6.0 km s^{-1}. Seismograms are bandpass filtered 1–30 Hz.

few observable phases. Its close location to the Lindau event makes comparison more easy.

4.1 Cortaillod earthquake

On 2006 March 29, the Cortaillod event occurred close to the town of Cortaillod in western Switzerland. It had a local magnitude (M_L) of 3.2 and was recorded at many stations which led to a good azimuthal coverage (azimuthal gap, GAP: 88°). Due to a missing nearby station (the closest station was 18 km away), the focal depth was originally not well constrained. Relocations based on a 3-D velocity model (Husen *et al.* 2003) and all available observations resulted in a focal depth of 6 km (Baer *et al.* 2007). Limiting the observations to *Pg* phases from stations up to around 70 km epicentral distance led to a focal depth of 9–10 km (Baer *et al.* 2007). The existence of strong surface waves and the fact that this region is known for shallow earthquakes argue for a shallower depth. A nearby earthquake whose depth is very well constrained based on the *S–P* traveltime of a 2-km distant station was located at 2-km depth. Since the *Pg*/*Pn* crossover distance for both events along cross-sections is the same, Baer *et al.* (2007) argued that the Cortaillod events must be at the same depth of 2 ± 1 km.

Based on the location with 20 *Pg* phases within the critical distance (Section 3.2 and Fig. 8), we add another nine *Pn* phases (stations OG10, PLONS, VDL, OG08, GUT, DAVOX, OG13, FUORN, OG16) that are far beyond the crossover distance. In this way, we avoid phases from the triplication zone where phase association can be difficult. Fig. 10 shows that we now get a location that is at a similar depth (around 9 km), but, as already discussed in Section 3.3, with an increased location precision which is the result of the improved range of take-off angles by the *Pn* phases. Compared to the focal depth of Baer *et al.* (2007) our location is too deep (Table 3). As the hypocentre and some of the stations are situated in the Molasse Basin, a reason for the too deep location could be the weak representation of the near-surface sediments in our velocity model. This is due to the poor resolution of the LET model close to the surface resulting in too high near-surface velocities in the model and, therefore, in a too deep earthquake location. Adding six secondary phases (*PmP*s at stations OG01, BBS, BALST, GDMS, LKBD, SALAN) our location has a similar precision, but is now much shallower (about 5 km; Fig. 10). The improved accuracy in this case can be attributed to the differential times between *Pg* and *PmP* phases which are less sensitive to the velocity model in terms of the poorly represented sediment velocities. The third location in Fig. 10 is based on all available observations excluding stations in the Molasse (TORNY, GIMEL, WIMIS, BALST, ACB, SLE, FLACH, ZUR, WILA) yielding a total of 39 observations. In this setup, we included some more further distant station readings to compensate for stations that were left out (Fig. 10). Whereas the GAP in all locations is the same (around 81°), the minimal station–epicentre distance increased from about 16–31 km. The new focal depth of about 3 km emphasizes the further increased accuracy while the precision is of similar quality. This result shows that the velocity model has indeed an effect, but it is not as strong as could be expected. Within the location uncertainties this focal depth is in agreement with the result of Baer *et al.* (2007).

4.2 Basel earthquake

The earthquake with a local magnitude (M_L) of 3.2 that occurred in the city of Basel (northern Switzerland) on 2007 February 2 was induced by the stimulation of an enhanced geothermal system

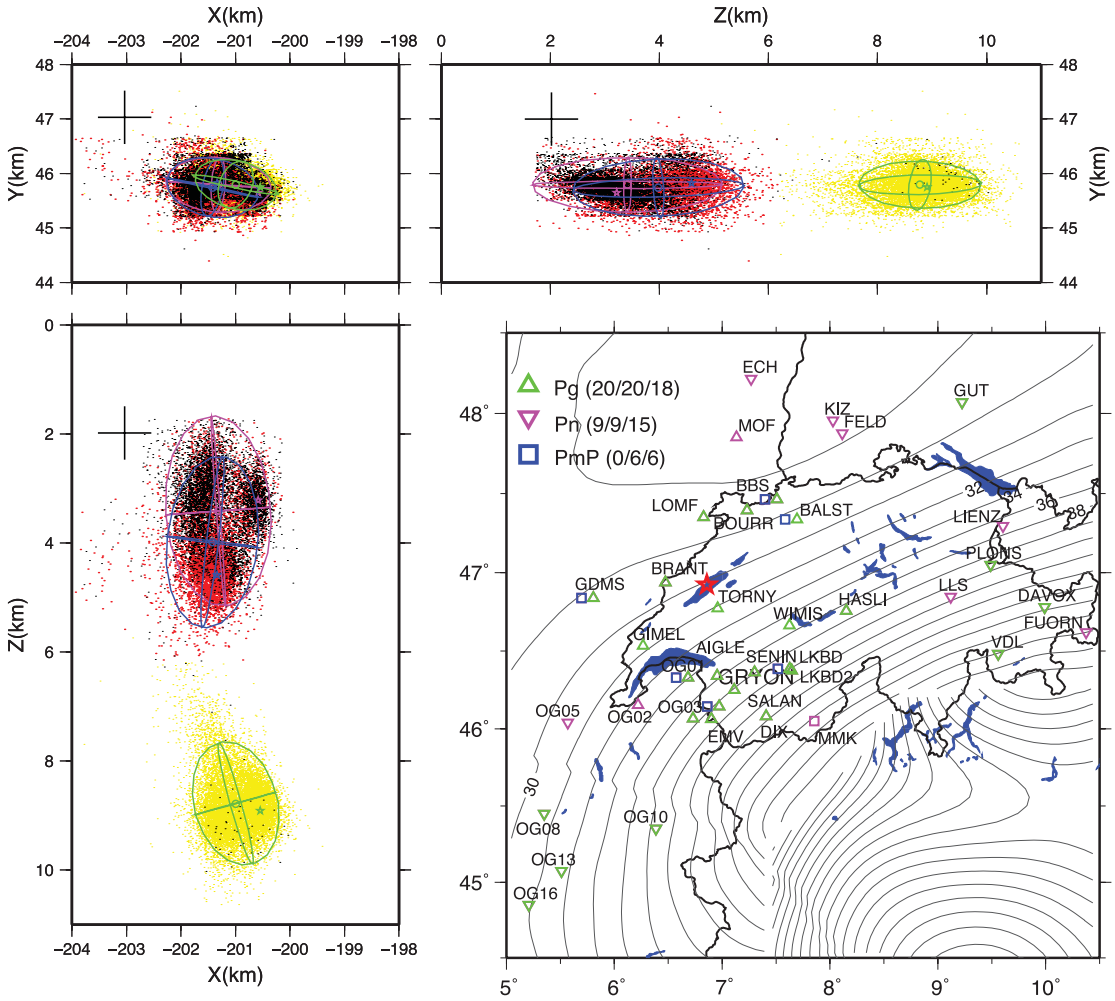

Figure 10. Posterior probability density function shown as density scatterplots for the Cortaillod earthquake computed using different phase combinations: yellow: *Pg* and *Pn* phases at all stations, red: *Pg, Pn, PmP* phases at all stations, black: *Pg, Pn, PmP* phases at stations that are not located in the Molasse Basin. Horizontal plane view and vertical cross-section in *x*-*z* direction and *y*-*z* direction are shown. Stars mark maximum likelihood locations. Projection of the 68 per cent confidence ellipsoids of each solution are shown by coloured lines: green: *Pg* and *Pn* phases at all stations; blue: *Pg, Pn, PmP* phases at all stations; pink: *Pg, Pn, PmP* phases at stations that are not located in the Molasse Basin. For each solution, origin time followed by geographical coordinates of the maximum likelihood hypocentre (Lat, Long, *Z*), root-mean-square of the residuals at the maximum likelihood location (rms), local magnitude (Mag), number of phases (Nphs), largest azimuthal gap in station distribution (Gap), distance of closest station to maximum likelihood epicentre location (Dist) are indicated. Colours represent different phase combinations as indicated. Black crosses show approximate location including uncertainties of Baer *et al.* (2007). Map in the lower right corner shows the earthquake epicentre (red star), the distribution of stations (different phases are marked by symbols and colours as indicated) and the Moho depth as 2 km contoured lines. Number of phases used in the different setups is indicated. See text for discussion of results.

below Basel. Due to precise information of the borehole depth, installed borehole seismometer and *S*–*P* traveltimes, Deichmann & Giardini (2009) could relocate the event using a relative master-event relocation technique with a very high accuracy and precision at a depth of 4 km (±0.1 km). The routine location of the Swiss Seismological Service of this event (absolute earthquake location), which includes only observations of nearby stations (up to about 12 km epicentral distance), is at a focal depth of 5 km (±1.2 km) (Deichmann & Giardini 2009). Since the event was strong enough to be recorded at many stations the number of observations and the azimuthal coverage are favourable.

Using a total number of 71 *Pg*, *Pn* and *PmP* phases at 64 stations where the closest one is at an epicentral distance of less than 1 km results in a precise location of the event at a focal depth of about 5 km (Fig. 11). This is only around 1 km deeper than the hypocentre location obtained by master-event relocation (Deichmann & Giardini 2009) and at the same depth as the routinely determined hypocentre location. Considering the location uncertainties, the routinely determined hypocentre location and our hypocentre location are in good agreement (Table 3 and Fig. 11). Taking into account that crustal phases of stations up to 230 km epicentral distance are used in our location, highlights the high consistency of computation of traveltimes in our 3-D *P*-wave model.

A reason for the deviation of the focal depth from the relatively determined location could be the poor resolution in our velocity model of the near-surface structure in the Upper Rhine Graben. Contrary to the Cortaillod event, where the earthquake was located in the sediments and some stations were also situated in the Molasse sediments, this earthquake occurred in the crystalline basement. Nevertheless, the situation in the Upper Rhine Graben with its sediments is similar to the Cortaillod case. Regarding the resolution of the velocity model, there are 26 stations in an epicentral distance of less than 15 km registering possibly unrealistic velocity variations that could influence the location of the earthquake as well.

Table 3. Focal depths of earthquakes discussed in Section 4.

Event	Location	Depth (km)
Cortaillod		
	Pg (first arr.), *Pn* (first arr.)	9 ± 0.6
	Pg (first arr.), *Pn* (first arr.), *PmP* (sec. arr.)	5 ± 0.8
	Pg (first arr.), *Pn* (first arr.), *PmP* (sec. arr.)—w/o stations molasse	3 ± 0.9
	Baer *et al.* (2007)	2 ± 1
Basel		
	Pg (first arr.), *Pn* (first arr.), *PmP* (sec. arr.)	5 ± 0.1
	Pg (first arr.), *Pn* (first arr.), *PmP* (sec. arr.)—w/o nearby stations	8 ± 0.5
	Deichmann & Giardini (2009), relative location	4 ± 0.1
	Deichmann & Giardini (2009), absolute location	5 ± 1.2
Lindau		
	Pg (first + sec. arr.)	28 ± 0.7
	Pg (first + sec. arr.), *Pn* (first arr.)	31 ± 0.1
	Baer *et al.* (2005)	31 ± 1.5
	Diehl *et al.* (2009a)	40 ± 4
Waldburg		
	Pg (first + sec. arr.), *Pn* (first arr.), *PmP* (sec. arr.)	30 ± 1.1
	Baer *et al.* (2003)	27 ± 5
	Diehl *et al.* (2009a)	36 ± 11

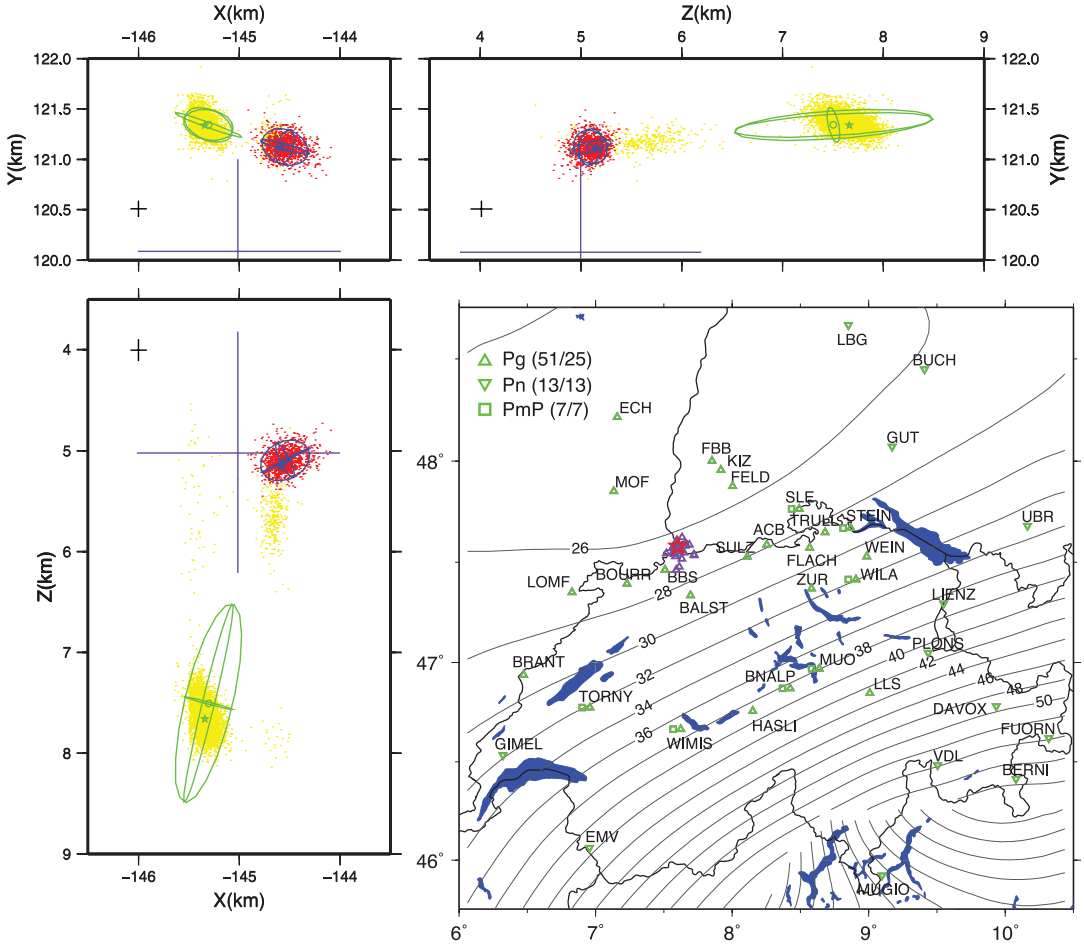

Figure 11. Same as Fig. 10, but for the Basel earthquake. Red dots, blue lines: *Pg, Pn* and *PmP* phases at all stations; yellow dots, green lines: *Pg, Pn* and *PmP* phases at stations at distances >15 km. Black crosses show approximate relative location including uncertainties of Deichmann & Giardini (2009); violet crosses show approximate routine location including uncertainties. See text for discussion of results.

Therefore, we removed those 26 closest stations which does not influence the GAP (64°) and relocated the event with the remaining 45 *Pg*, *Pn* and *PmP* phases resulting in a focal depth of 8 km. Fig. 11 shows that the epicentral location precision is comparable to the previous location, but the epicentre was shifted. The precision in focal depth decreased dramatically. The scatter density cloud (yellow dots) in Fig. 11 shows a second minimum that is more consistent with the *Pn* phases used in this location and also more

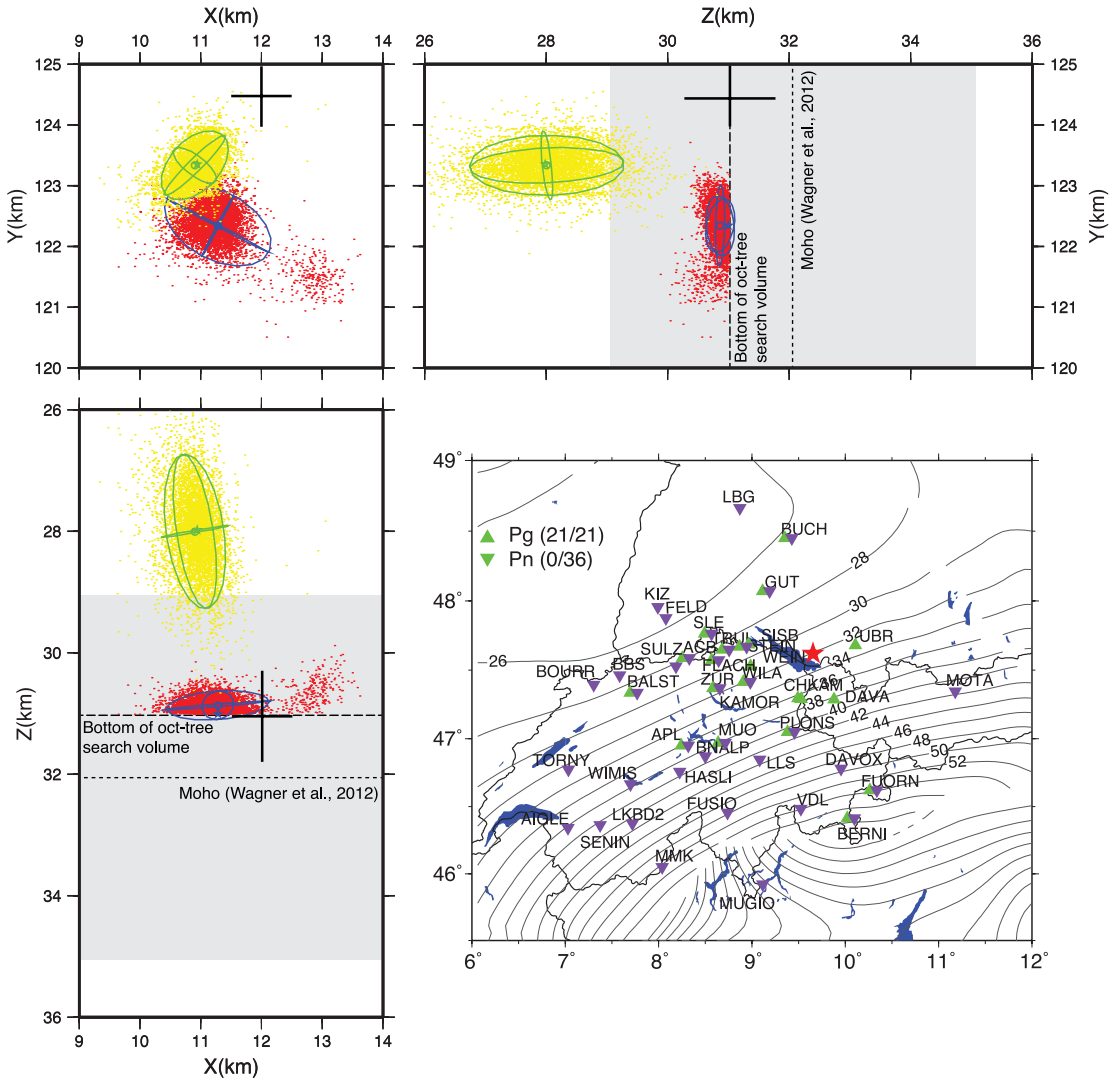

Figure 12. Same as Fig. 11, but for the Lindau earthquake. Red dots, blue lines: *Pg* and *Pn* phases at all stations; yellow dots, green lines: *Pg* phases at all stations. Short dashed lines mark Moho depth at maximum likelihood epicentre location. Long dashed lines mark bottom of oct-tree search volume at maximum likelihood epicentre location. Grey shaded area symbolizes minimum Moho depth uncertainty of ±3 km. Black crosses show approximate location including uncertainties of Baer *et al.* (2005). See text for discussion of results.

consistent with the previous location including all nearby stations. As a conclusion we can say that in this case the usage of secondary phases is not able to make up for the many nearby stations. This is a bit different to the Cortaillod event where on the one hand less stations were removed and on the other hand there was anyway no station in a distance of about 1.5 times the focal depth.

4.3 Lindau earthquake

In southern Germany, close to the Lake Constance, the earthquake of Lindau occurred with a local magnitude (M_L) of 3.0 on 2004 April 18. Baer *et al.* (2005) located the event routinely with a 1-D model at a depth of 29–33 km. Relocation with a 3-D model (Husen *et al.* 2003) resulted in a focal depth of 33 km (Baer *et al.* 2005). Based on *Pg*–*Pn* traveltime differences Baer *et al.* (2005) concluded that the event must be 1–2 km above the Moho discontinuity which they stated to be 32 km deep (Waldhauser *et al.* 1998). Thus, the hypocentre was fixed at a depth of 31 km. The uncertainty in focal depth is given as ±1.5 km (Baer *et al.* 2005).

Diehl *et al.* (2009a) relocated the Lindau earthquake with their LET *P*-wave velocity model as well. The result of a focal depth of 40 ± 4 km would argue for a location in the European mantle. Using velocity reduced record sections as, for example, described in Deichmann (1987) and Diehl *et al.* (2009b), they falsified the location in the mantle based on the presence of *PmP* phases that would not have been observed if the earthquake was not in the crust.

Relocating the earthquake with all available *Pg* phases (in total 21, thereof 6 first and 15 secondary arrivals) results in a fairly well-determined hypocentre with a focal depth of 28 km that is about 4–5 km above the Moho being at a depth of around 32–33 km in this area (Fig. 12). The existence of a station in about 36 km epicentral distance certainly contributes to the good constraint in focal depth. Adding the remaining *Pn* phases we can now relocate the event with a total number of 57 observations that results in a focal depth of 31 km at the bottom of the oct-tree search volume, shifted to SSE (about 1.0 km to the south and 0.3 km to the east) compared to the previous location (Fig. 12). The scatter density cloud indicates a compact PDF which is smaller in vertical than in horizontal direction, but cut at the bottom of the oct-tree search

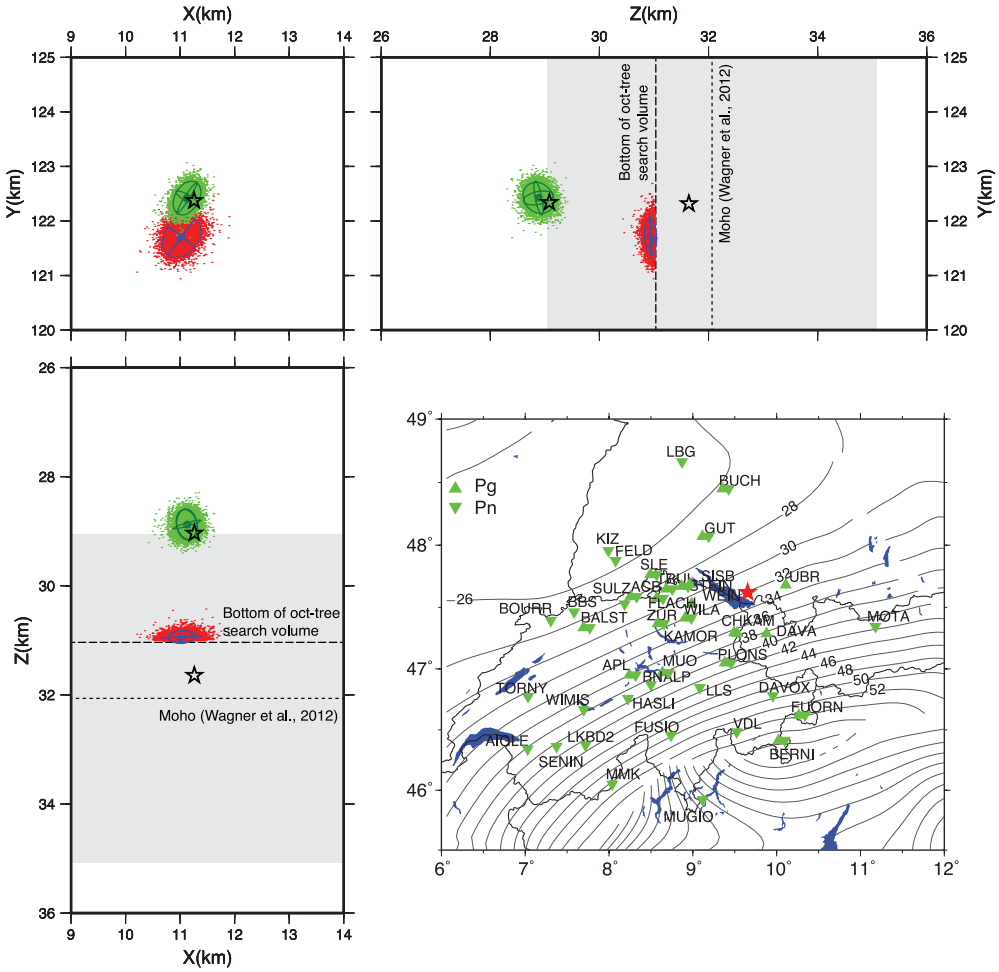

Figure 13. Same as Fig. 12, but for a synthetic test using the number and phases of the 2004 Lindau earthquake. True hypocentre location (black star) is located at 29 km depth within oct-tree search volume (green scatter density cloud) and 31.6 km depth below oct-tree search volume (red scatter density cloud). See text for discussion of results.

volume. In the FMM procedure, traveltimes are computed and stored on equally spaced grid nodes of the so-called propagation grid (see Section 3.2). Traveltimes are also correctly computed for grid nodes along the Moho interface, but these are not stored. Since the location PDF can only be computed at those grid nodes, for which traveltimes have been computed, the search volume of the oct-tree search is limited in vertical direction by the grid nodes of the propagation grid closest to the Moho. Given our vertical grid nodes spacing of 2 km the search volume of the oct-tree search stops a maximum distance of 2 km to the Moho, or at 31 km in the case of the Lindau earthquake.

We tested the effect of a limited search volume on the location PDF by relocating synthetic earthquakes, for which the true hypocentre location was within and below the oct-tree search volume (Fig. 13). We used the real station distribution of the Lindau earthquake for these tests. As expected, hypocentre location and location PDF were correctly recovered if the true hypocentre location was within the oct-tree search volume (Fig. 13, green scatter density cloud). The location PDF was cut in vertical direction if the true hypocentre location was outside the oct-tree search volume (Fig. 13, red scatter density cloud). Focal depth was estimated very close to the bottom of the oct-tree search volume. We also observed a slight shift in epicentre location (<200 m) which is due to the coupling of epicentre location and focal depth. Our results resemble those obtained from real data of the 2004 Lindau earthquake (Fig. 12). We, therefore, interpret our results as such that focal depth estimates will cluster close to the bottom of the oct-tree search volume if the true hypocentre location is close to the Moho, that is within 2 km. Given a minimum uncertainty of ±3 km in Moho depth (Waldhauser *et al.* 1998) we think that the bias introduced in focal depth of maximum 2 km by limiting the oct-tree search volume is insignificant in terms of accuracy. It should be noted, however, that location uncertainties derived from the scatter density clouds are unreliable since they are based on a location PDF that is cut by the bottom of the oct-tree search volume.

4.4 Waldburg earthquake

On 2002 July 6, the second deep crustal earthquake shown in this study occurred in southern Germany, close to the city of Waldburg, with a local magnitude (M_L) of 3.1. Similar to the previously discussed 2004 Lindau event, Diehl *et al.* (2009a) relocated this earthquake with their LET model resulting in a focal depth of 36 ± 11 km. Based on velocity reduced record sections and the presence of *Pn* and *PmP* phases, they again argued for a location in the European crust just above the Moho that is at a depth of about 31 km in this region (Wagner *et al.* 2012). In this way, their location is also in accordance to the result of Baer *et al.* (2003) who relocated the event at a depth of 27 ± 5 km.

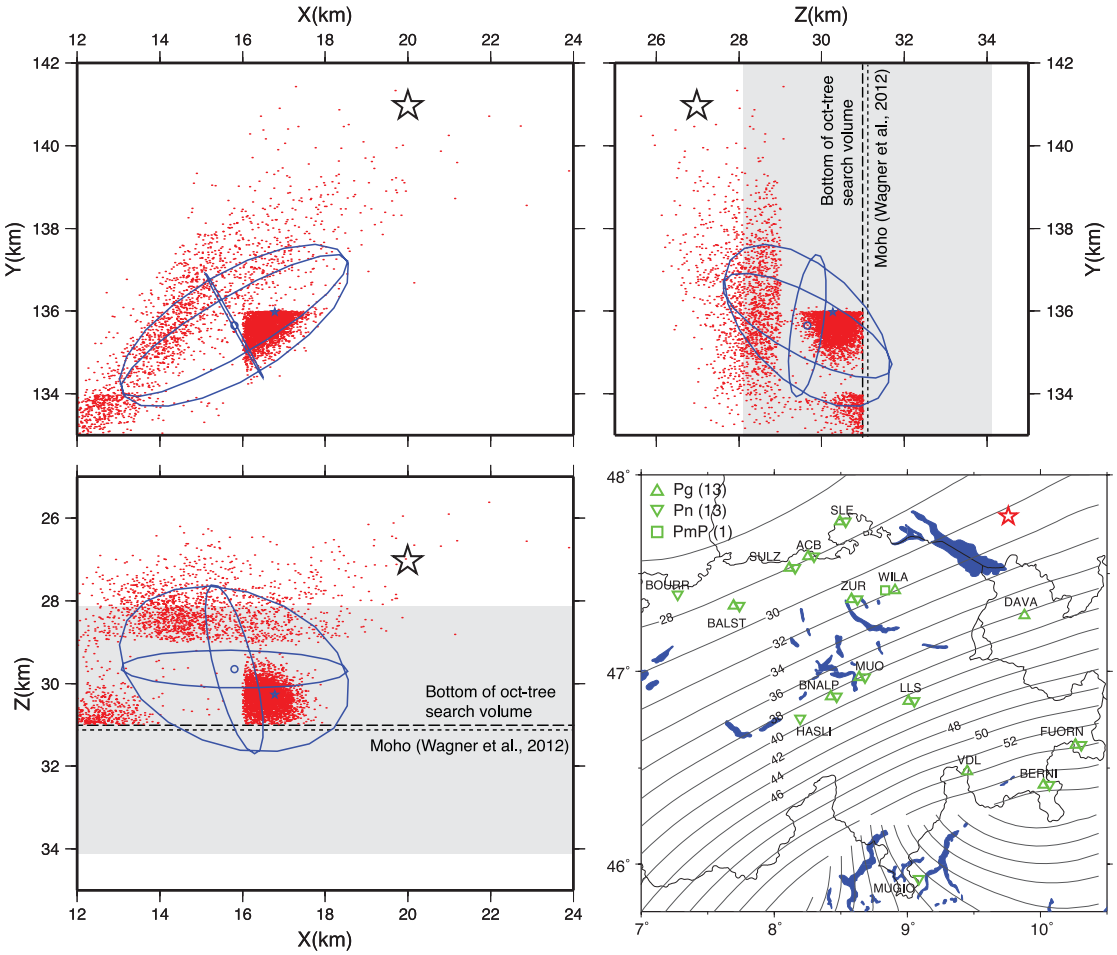

Figure 14. Same as Fig. 12, but for the Waldburg earthquake. Only one solution using all available phases was computed. Black stars show approximate location of Baer *et al.* (2003). Location uncertainties of Baer *et al.* (2003) are not shown due to their size. See text for discussion of results.

With an unfavourable station geometry (GAP: 248°) and a total number of 27 observations (13 *Pg*, 13 *Pn*, 1 *PmP*) we could relocate this earthquake at a depth of 30 km. The location PDF is very complex and, thus, not very well represented by the 68 per cent confidence ellipsoid (Fig. 14). The complex topology of the location PDF is likely a result of the unfavourable station geometry in combination with the local Moho topography. Similar to the 2004 Lindau earthquake the location PDF is cut by the bottom of the oct-tree search volume, which shows a 2-km step in this region (Fig. 14). As the closest station is about 50 km away focal depth is not very well constraint, but secondary phases and *a priori* information about the crust–mantle boundary help to constrain the focal depth in relation to the Moho. The unfavourable distribution of stations (GAP: 248°) is responsible for the poorly constraint epicentral location, which cannot be compensated by the use of secondary phases. Within the given uncertainties our hypocentre location is in accordance with the results of Baer *et al.* (2003) and Diehl *et al.* (2009a).

5 DISCUSSION AND CONCLUSION

The application of 3-D velocity models to compute traveltimes of secondary phases and a non-linear representation of the earthquake location problem are a good approach to precisely determine earthquake hypocentres. In global teleseismic earthquake location, secondary phase information is already included, but usually only 1-D velocity models are used (e.g. Engdahl *et al.* 1998). The routine location of regional earthquakes is sometimes based on 3-D velocity models (e.g. Husen *et al.* 2003), but since these models are mainly LET models, parametrization restrictions prevent modelling of a sharp crust mantle boundary and, thus, the calculation of traveltimes of secondary phases. Interactive 2-D ray tracing approaches including secondary phases are good to constrain the focal depth of individual events (e.g. Garcia Fernandez & Mayer-Rosa 1986; Deichmann 1987; Baer *et al.* 2003, 2007; Kastrup *et al.* 2007), but they are quite time-consuming and again based on simplified 1-D velocity models that cannot fully represent the sometimes highly complex 3-D variations in seismic velocities and Moho topography.

A disadvantage of our newly developed approach is that the identification and association of additional phases will demand more time before the event may be located. As we compute traveltimes of first and secondary arrivals, that is *Pg*, *Pn* and *PmP* phases, a correct association of phases is essential. However, this extra time is rewarded with more accurate and precise earthquake locations.

The beneficial usage of secondary phases for the earthquake location was demonstrated by synthetic tests (Section 3.3) and for some real earthquake examples (Section 4). Our relocation tests using synthetic data (Section 3.3) showed that the use of *Pn* and *PmP* phases improves location precision not only because they increase the total number of observations, which is especially useful when only a few observations are available, but also because they improve the range of available take-off angles. Thus, the beneficial effect of

secondary arrivals is that they leave the source with different take-off angles compared to first arriving *Pg* or *Pn* phases. Gomberg *et al.* (1990) showed how *S* phases can put important constraints on the focal depth by geometrically travelling like a *P* phase, but with a steeper angle to a closer station. Having in mind that a station in about 1.4 focal depth's distance drastically improves the determination of focal depth, one can clearly see the importance of *S* phases. On the other side, Gomberg *et al.* (1990) also conclude that due to its strong influence on the determination of the focal depth, a wrong *S* phase pick at a close station results in a very stable, but wrong solution. Moreover, systematic *S* phase timing errors still result in an increased precision, but entail decreased accuracy. Similar considerations can be taken into account when secondary *P* phases are used for the earthquake location, namely an improved range of take-off angles and differential traveltimes of phases at the same station. A further advantage of *PmP* phases is that they neither need to be picked on rotated seismograms, nor require rarely existing *S*-wave models or often inaccurate *P* wave to *S*-wave velocity (*Vp*/*Vs*) ratios. A disadvantage of *PmP* and *Pn* phases is that they are very sensitive to Moho topography and seismic velocities in the lower crust and, thus, lead to a similar situation as wrongly determined *S* phases, by increasing the location precision while decreasing its accuracy if a wrong velocity model is used for relocation (see Section 3.3, Tables 1 and 2).

In our current approach, the search volume of the oct-tree search is limited close to the Moho interface. This limitation is a consequence of using regularly spaced traveltime grids in NonLinLoc and irregularly spaced interface grids in the FMM procedure. As a result, hypocentre locations that locate beneath the bottom of the oct-tree search volume but above the Moho interface will be located close to the bottom of the oct-tree search volume with a location PDF that is cut. In terms of location accuracy, this limitation is insignificant since our vertical grid node spacing of 2 km is less than the minimum uncertainty in Moho depth of ± 3 km. It should be noted, though, that location uncertainties derived from scatter density clouds, such as the 68 per cent confidence ellipsoid, become unreliable. To overcome this problem would either require a smaller vertical grid node spacing, which would significantly increase computation time, or the use of irregularly spaced traveltime fields in NonLinLoc, which would require significant changes to the code.

Since identification of phases and picking of the correct onsets become very important in our approach, there should be some time invested in developing tools that can assist in this work. Diehl *et al.* (2009b) introduced a probabilistic approach of determining arrival times and their uncertainties for first arriving phases. Their method is based on the idea of detecting the 'most likely' phase onset that will have the highest probability. Consequently, the 'earliest' and 'latest' possible phase onsets define the outer limits (zero probability) of an interval including the possible phase onset. It is straightforward to apply the approach of Diehl *et al.* (2009b) to *PmP* phases too. In addition, our model could be used to calculate predicted arrival times providing further support.

The influence of poorly represented near-surface velocities in the model on the earthquake location was partly shown on the location of the Cortaillod event in Section 4. As a consequence it is important to further improve the velocity model by incorporating near-surface information based on CSS. It is also of high interest to develop an independent *S*-wave velocity model which will further increase the determination of earthquake hypocentres, especially when only a few phase readings are existing. The construction of such a *S*-wave model should be possible in a similar way as it was done for our *P*-wave model, provided enough high-quality *S*-wave data are available. Since the *S* body wave information remains sparse, however, ambient noise models could be a key to such a model (see, e.g. Verbeke *et al.* 2012).

Nevertheless, already our 3-D crustal *P*-wave velocity model in combination with secondary phases is a significant step forward for the earthquake location. The parametrization of the model with a true first-order Moho discontinuity that allows for the computation of secondary phases is a great benefit. *A priori* constraints such as the existence of Moho reflected phases (*PmP*) further improve the accuracy of the hypocentre, especially when locating deep earthquakes that occurred close to the Moho discontinuity. The limitation in the oct-tree search volume, which is an issue if the earthquake is located between the bottom of the search volume and the Moho (see Section 4), is insignificant in terms of accuracy, because of an minimum uncertainty in Moho depth of ± 3 km. By investigating deep crustal events, our method can help in the discussion whether earthquakes occur in the crust or in the mantle and, thus, can make the case for a specific rheological model (e.g. Maggi *et al.* 2000; Priestley *et al.* 2008).

ACKNOWLEDGEMENTS

We thank I. Grevemeyer and two anonymous reviewers whose thoughtful remarks and recommendations greatly improved the manuscript. The Generic Mapping Tools by Wessel & Smith (1998) were used to generate most of the figures.

REFERENCES

Baer, M. *et al.*, 2003. Earthquakes in Switzerland and surrounding regions during 2002, *Eclogae Geol. Helv.,* **96**(2), 313–324.

Baer, M. *et al.*, 2005. Earthquakes in Switzerland and surrounding regions during 2004, *Eclogae Geol. Helv.,* **98**(3), 407–418.

Baer, M. *et al.*, 2007. Earthquakes in Switzerland and surrounding regions during 2006, *Swiss J. Geosci.,* **100**(3), 517–528.

Bai, C.-y., Huang, G.-j. & Zhao, R., 2010. 2-D/3-D irregular shortest-path ray tracing for multiple arrivals and its applications, *Geophys. J. Int.,* **183**(3), 1596–1612.

Bondár, I., Yang, X., North, R. & Romney, C., 2001. Location calibration data for CTBT monitoring at the Prototype International Data Center, *Pure appl. Geophys.,* **158**(1), 19–34.

Bondár, I. *et al.*, 2004. Collection of a reference event set for regional and teleseismic location calibration, *Bull. seism. Soc. Am.,* **94**(4), 1528–1545.

Cattaneo, M., Augliera, P., Parolai, S. & Spallarossa, D., 1999. Anomalously deep earthquakes in northwestern Italy, *J. Seismol.,* pp. 421–435.

Chen, W.-P. & Molnar, P., 1983. Focal depths of intracontinental and intraplate earthquakes and their implications for the thermal and mechanical properties of the lithosphere, *J. geophys. Res.,* **88**(B5), 4183–4214.

de Kool, M., Rawlinson, N. & Sambridge, M., 2006. A practical grid-based method for tracking multiple refraction and reflection phases in three-dimensional heterogeneous media, *Geophys. J. Int.,* **167**(1), 253–270.

Deichmann, N., 1987. Focal depths of earthquakes in northern Switzerland, *Ann. Geophys.,* **5B,** 395–402.

Deichmann, N., 1992. Structural and rheological implications of lower-crustal earthquakes below northern Switzerland, *Phys. Earth planet. Inter.,* **69**(34), 270–280.

Deichmann, N. & Baer, M., 1990. Earthquake focal depth below the Alps and northern Alpine foreland of Switzerland, in *The European Geotraverse: Integrative Studies,* pp. 277–288, eds Freeman, R., Giese, P. & Mueller, St., European Science Foundation, Strasbourg.

Deichmann, N. & Giardini, D., 2009. Earthquakes induced by the stimulation of an enhanced geothermal system below Basel (Switzerland), *Seism. Res. Lett.,* **80**(5), 784–798.

Deichmann, N. *et al.*, 2008. Earthquakes in Switzerland and surrounding regions during 2007, *Swiss J. Geosci.,* **101**(3), 659–667.

Diehl, T., Husen, S., Kissling, E. & Deichmann, N., 2009a. High-resolution 3-D P-wave model of the Alpine crust, *Geophys. J. Int.,* **179**(2), 1133–1147.

Diehl, T., Kissling, E., Husen, S. & Aldersons, F., 2009b. Consistent phase picking for regional tomography models: application to the greater Alpine region, *Geophys. J. Int.,* **176**(2), 542–554.

Engdahl, E., van der Hilst, R. & Buland, R., 1998. Global teleseismic earthquake relocation with improved travel times and procedures for depth determination, *Bull. seism. Soc. Am.,* **88**(3), 722–743.

Font, Y., Kao, H., Lallemand, S., Liu, C.-S. & Chiao, L.-Y., 2004. Hypocentre determination offshore of eastern Taiwan using the Maximum Intersection method, *Geophys. J. Int.,* **158**(2), 655–675.

Garcia Fernandez, M. & Mayer-Rosa, D., 1986. Improved hypocentral parameter determination using secondary regional phases, *Rev. Geofis.,* **42,** 175–184.

Gomberg, J., Shedlock, K. & Roecker, S., 1990. The effect of S-wave arrival times on the accuracy of hypocenter estimation, *Bull. seism. Soc. Am.,* **80**(6A), 1605–1628.

Haslinger, F. & Kissling, E., 2001. Investigating effects of 3-D ray tracing methods in local earthquake tomography, *Phys. Earth planet. Inter.,* **123**(2–4), 103–114.

Husen, S., Kissling, E., Deichmann, N., Wiemer, S., Giardini, D. & Baer, M., 2003. Probabilistic earthquake location in complex three-dimensional velocity models: application to Switzerland, *J. geophys. Res.,* **108**(B2), 2077, doi:10.1029/2002JB001778.

Kastrup, U., Deichmann, N., Fröhlich, A. & Giardini, D., 2007. Evidence for an active fault below the northwestern Alpine foreland of Switzerland, *Geophys. J. Int.,* **169**(3), 1273–1288.

Kissling, E., 1993. Deep structure of the Alps—what do we really know? *Phys. Earth planet. Inter.,* **79**(1–2), 87–112.

Kissling, E., Ellsworth, W., Eberhart-Phillips, D. & Kradolfer, U., 1994. Initial reference models in local earthquake tomography, *J. geophys. Res.,* **99**(B10), 19 635–19 646.

Kissling, E., Husen, S. & Haslinger, F., 2001. Model parametrization in seismic tomography: a choice of consequence for the solution quality, *Phys. Earth planet. Inter.,* **123,** 89–101.

Lomax, A., 2005. A reanalysis of the hypocentral location and related observations for the Great 1906 California earthquake, *Bull. seism. Soc. Am.,* **95**(3), 861–877.

Lomax, A., Virieux, J., Volant, P. & Berge-Thierry, C., 2000. Probabilistic earthquake location in 3D and layered models, in *Advances in Seismic Event Location,* Chap. 5, pp. 101–134, eds Thurber, C.H. & Rabinowitz, N., Kluwer Academic Publishers, Dordrecht/Boston/London.

Luetgert, J.H., 1992. *MacRay—interactive two-dimensional seismic raytracing for the Macintosh, Tech. rep.,* U.S. Geological Survey, Menlo Park, California.

Ma, S., 2010. Focal depth determination for moderate and small earthquakes by modeling regional depth phases sPg, sPmP, and sPn, *Bull. seism. Soc. Am.,* **100**(3), 1073–1088.

Maggi, A., Jackson, J.A., Mckenzie, D. & Priestley, K., 2000. Earthquake focal depths, effective elastic thickness, and the strength of the continental lithosphere, *Geology,* **28,** 495–498.

Mueller, S., 1977. A new model of the continental crust, in *The Earth's Crust,* Vol. 20: Geophysical Monograph, pp. 727–747, Am. Geophys. Union.

Podvin, P. & Lecomte, I., 1991. Finite difference computation of traveltimes in very contrasted velocity models: a massively parallel approach and its associated tools, *Geophys. J. Int.,* **105**(1), 271–284.

Priestley, K., Jackson, J. & McKenzie, D., 2008. Lithospheric structure and deep earthquakes beneath India, the Himalaya and southern Tibet, *Geophys. J. Int.,* **172**(1), 345–362.

Quin, H.R. & Thurber, C.H., 1992. Seismic velocity structure and event relocation in Kazakhstan from secondary P phases, *Bull. seism. Soc. Am.,* **82**(6), 2494–2510.

Rawlinson, N. & Sambridge, M., 2004a. Wave front evolution in strongly heterogeneous layered media using the fast marching method, *Geophys. J. Int.,* **156**(3), 631–647.

Rawlinson, N. & Sambridge, M., 2004b. Multiple reflection and transmission phases in complex layered media using a multistage fast marching method, *Geophysics,* **69**(5), 1338–1350.

Rawlinson, N. & Sambridge, M., 2005. The fast marching method: an effective tool for tomographic imaging and tracking multiple phases in complex layered media, *Explor. Geophys.,* **36**(4), 341–350.

Schmid, S.M. & Kissling, E., 2000. The arc of the western Alps in the light of geophysical data on deep crustal structure, *Tectonics,* **19**(1), 62–85.

Storchak, D., Schweitzer, J. & Bormann, P., 2003. The IASPEI standard seismic phase list, *Seism. Res. Lett.,* **74**(6), 761–772.

Stroujkova, A., 2009. Constraining event depths and crustal velocities using regional depth phases, *Bull. seism. Soc. Am.,* **99**(1), 215–225.

Verbeke, J., Boschi, L., Stehly, L., Kissling, E. & Michelini, A., 2012. High-resolution Rayleigh-wave velocity maps of central Europe from a dense ambient-noise data set, *Geophys. J. Int.,* **188,** 1173–1187.

Wagner, M., Kissling, E. & Husen, S., 2012. Combining controlled-source seismology and local earthquake tomography to derive a 3-D crustal model of the western Alpine region, *Geophys. J. Int.,* **191,** 789–802.

Waldhauser, F., Kissling, E., Ansorge, J. & Mueller, S., 1998. Three-dimensional interface modelling with two-dimensional seismic data: the Alpine crust-mantle boundary, *Geophys. J. Int.,* **135**(1), 264–278.

Waldhauser, F., Lippitsch, R., Kissling, E. & Ansorge, J., 2002. High-resolution teleseismic tomography of upper-mantle structure using an a priori three-dimensional crustal model, *Geophys. J. Int.,* **150**(2), 403–414.

Wessel, P. & Smith, W. H.F., 1998. New, improved version of the Generic Mapping Tools released, *EOS, Trans. Am. geophys. Un.,* **79**(47), 579.